

AN ABSTRACT OF THE THESIS OF

Michael B. Hager for the degree of Master of Science in Mechanical Engineering  
presented on December 10, 1996. Title: Advanced Numerical Modeling of the Lorentz  
Mixing Process

Abstract Approved:

Redacted for Privacy

Heidi A. Pattee

There are numerous techniques for improving the mixing of fuel and oxidant species. However, many of these methods cannot be applied to combustion systems due to material limitations. A means of mixing the reacting species without physically invading the flow stream is therefore desired.

In this work, induced electromagnetic forces known as Lorentz forces are considered as a means of enhancing the combustion of co-flowing reactant streams. To evaluate the effect of various parameters on the mixing process, a non-dimensional description is derived and used to develop a numerical model. Numerical experiments are performed based on a three level Box-Behnken design in which the dimensionless Lorentz force parameter, Reynolds number, and Euler number are varied.

The Lorentz force parameter has a large effect on the mixing process. The Reynolds number has a minor effect on mixing, and the Euler number has a negligible effect. Confirmation of these results through experimental work is needed. Approaches that could be used to verify these results experimentally are outlined, and the construction and testing of a burner suitable for further experiments on Lorentz mixing is described.

**Advanced Numerical Modeling of the  
Lorentz Mixing Process**

by

**Michael B. Hager**

**A THESIS**

submitted to

**Oregon State University**

in partial fulfillment of  
the requirements for the  
degree of

**Master of Science**

Presented December 10, 1996  
Commencement June 1997

Master of Science thesis of Michael B. Hager presented on December 10, 1996

APPROVED:

Redacted for Privacy

---

Major Professor, representing Mechanical Engineering

Redacted for Privacy

---

Head of Department of Mechanical Engineering

Redacted for Privacy

---

Dean of Graduate School

I understand that my thesis will become part of the permanent collection of Oregon State University libraries. My signature below authorizes release of my thesis to any reader upon request.

Redacted for Privacy

---

Michael B. Hager, Author

## TABLE OF CONTENTS

	<u>Page</u>
BACKGROUND.....	1
Previous Work.....	1
Motivation.....	2
Acknowledgments.....	3
THEORETICAL DEVELOPMENT.....	4
Conservation Equations.....	4
Dimensional Analysis.....	7
NUMERICAL IMPLEMENTATION.....	11
Description of the Lorentz Force .....	11
Computational Domain.....	19
Fluid Flow.....	23
Species Diffusion.....	25
Turbulence.....	26
NUMERICAL RESULTS.....	29
Code Validation.....	29
Design of Experiments.....	33
Numerical Results.....	35
APPLICATIONS.....	38
Burner Design.....	38
Redesigned Burner.....	42
Seeding System.....	46

TABLE OF CONTENTS  
(Continued)

	<u>Page</u>
Design Summary.....	48
Proposed Experiments.....	49
SUMMARY.....	51
BIBLIOGRAPHY.....	53
APPENDICES.....	55
APPENDIX A: UCODE3 Input File.....	56
APPENDIX B: Input file generating Code.....	58
APPENDIX C: CFD Code.....	61

## LIST OF FIGURES

<u>Figure</u>		<u>Page</u>
3.1	Replace electrodes with ideal charged spheres.	12
3.2	Comparison of electric field for an infinite parallel-plate capacitor with Eq. (28).	14
3.3	FE mesh and lines of constant electric field.	16
3.4	Comparison of Eq. (28) with 3mm FE solution.	17
3.5	Correlation of ideal sphere diameter with electrode diameter used in FE solutions for a fixed distance between spheres of 2 cm.	18
3.6	Computational domain defined as equipotential plane between electrodes.	19
3.7	(a) Normal grid with all variables defined at coincident (i,j) grid points and (b) staggered grid with scalar variables defined at (i,j) grid points and vector quantities defined on cell faces centered about (i,j) grid points.	20
3.8	Staggering of continuity and momentum cells. fluxing quantity and (b) a negative fluxing quantity of y-momentum equation.	21
3.9	Velocities used to compute flux terms of X-momentum equation.	22
3.10	Contours of turbulent viscosity with maximum value of $9.1e-4$ occurring nearest the channel walls.	28
3.11	Contours of turbulent viscosity within the channel. Maximum value shown of $1.0e-6$ occurs nearest channel walls.	28
4.1	Comparison of analytical and numerical solutions.	30
4.2	Developing velocity profiles for a flow with $Re = 10$ and $Eu = 1$ .	31
4.3	Non-dimensional pressure drop vs. distance downstream for dual inlet flow over (a) developing region and (b) full length of channel.	32
4.4	Developing velocity profiles for dual inlet flow.	33

LIST OF FIGURES  
(Continued)

<u>Figure</u>		<u>Page</u>
4.5	Species concentration for flows with $Eu = 1$ and $\Pi_1 = 10$ .	36
4.6	Main effects plot for non-dimensional flow parameters.	37
4.7	Interactions plot for non-dimensional parameters.	37
5.1	Machined ceramic block used to form flow channels.	40
5.2	Drawing of assembled prototype burner.	41
5.3	Flow channel assembly.	42
5.4	Base with guide veins and gas inlet ports.	43
5.5	Two-part adjustable electrode mount and assembly.	44
5.6	Burner with and without shroud.	45
5.7	Laminar flame sheet.	45
5.8	Schematic of seeding chamber.	47
5.9	Schematic of PLIF experiment.	49

## NOMENCLATURE

<b>B</b>	Magnetic flux density vector.
$C_n$	Concentration of species n.
$C_o$	Inlet concentration.
$c_p$	Specific heat.
<b>D</b>	Diameter of electrodes.
$D_{n\leftrightarrow n}$	Binary diffusion coefficient.
$D_p$	Width of flow channel.
$D_t$	Turbulent diffusion coefficient.
<b>E</b>	Electric field vector.
$Eu_\omega$	Euler number.
$e_i$	Unit vectors.
<b>f</b>	Body force vector.
$Fr_\omega$	Froude number.
<b>g</b>	Gravitational force vector.
<b>i</b>	Number of nodes for flow development.
<b>I</b>	Entrance length for flow development.
<b>J</b>	Current density vector.
$k_t$	Turbulent thermal conductivity.
<b>l</b>	Reference distance for turbulence model.
<b>Le</b>	Lewis number.
<b>P</b>	Pressure.
<b>q</b>	Quantity of charge.
<b>r</b>	Position vector.
$Re_\omega$	Reynolds number.
$R_h$	Hartman number.
$R_H$	Magnetic pressure number.
$R_m$	Magnetic number.
<b>t</b>	Time.
$t_o$	Time when predicted values are made.
$u, \mathbf{u}$	X-component of velocity.
$U_{ref}$	Reference velocity.
$v, \mathbf{v}$	Y-component of velocity.
<b>V</b>	Voltage (scalar potential).
<b>x, y, z</b>	Cartesian coordinates.
$z_o$	Distance from origin to center of ideal charged spheres.
$\beta$	Pressure solution variable.
$\delta$	Radius of ideal charged sphere.
$\delta t$	Time step used for diffusion computations.
$\Delta P$	Pressure drop.
$\Delta t$	Time step used in for fluid flow computations.
$\Delta V$	Voltage drop.

NOMENCLATURE  
(Continued)

$\Delta x, \Delta y$	Grid spacing in x and y-directions.
$\epsilon_0$	Permeativity of free space.
$\mu$	Fluid viscosity.
$\mu_0$	Permeability of free space.
$\mu_t$	Turbulent viscosity.
$\mu_w$	Viscosity at the channel wall.
$\rho, \rho_w$	Fluid density, density near wall (same).
$\Pi_1$	Non-dimensional Lorentz force parameter.
$\sigma$	Electrical conductivity of fluid.
$\tau_w$	Fluid shear stress near wall.
$\omega$	Electric field oscillation frequency.
$\omega$	Vorticity vector.
$\chi$	Non-dimensional species concentration.

# Advanced Numerical Modeling of the Lorentz Mixing Process

## BACKGROUND

Combustion of hydrocarbon fuels has applications in almost every aspect of our lives. The chemical reactions of the combustion process can take place with fuels either premixed or non-premixed. Premixed combustion is limited primarily by chemical reaction rates while non-premixed combustion is limited by molecular diffusion of the fuel and oxidizer species. In addition, premixing of fuel and oxidant usually results in cleaner combustion. However, not all applications are suited for premixed combustion. Combustion of volatile fuels, for example, can result in dangerous conditions and premixing is avoided. It is desired to enhance the combustion of diffusion flames under such circumstances. Mixing of the fuel and oxidant species at the time of combustion is a difficult task. Many techniques for improving the mixing (e.g. placing an object in the flow stream to promote turbulence) cannot be easily applied to combustion systems due to material limitations. It is therefore desired to develop a means of mixing the reacting species without physically invading the flow stream. It is the goal of this project to evaluate the use of Lorentz forces to enhance the combustion of co-flowing reactant streams.

### Previous Work

Pattee and Peterson (1993) investigated a new technique for enhancing bulk mixing in planar diffusion flames. A voltage was applied across electrodes to create an electric current through a flame sheet. A uniform magnetic field was applied and, due to the orientation of the fields, a Lorentz force was induced. Their work consisted of

comparing theoretical predictions of the lateral velocity experienced by the flame sheet with high-speed video images of experimental flames. This work provided the motivation for investigating the Lorentz mixing process.

Thompson (1994) performed numerical simulations of alkali seeded diffusion flames subjected to Lorentz forces. His model used a predictor-corrector scheme to solve for the flow field of an incompressible, isothermal gas. Many assumptions about the field strengths were used and results of viscous effects were not shown.

### Motivation

The experimental work of Pattee and Peterson and the CFD modeling of Thompson formed a starting point for the present work on the subject of Lorentz mixing. Pattee and Peterson demonstrated the important ability to create appreciable Lorentz Forces in the laboratory and Thompson demonstrated the usefulness of CFD solutions as a visualization tool.

The computational model developed by Thompson enabled visualization of the effect of a time-varying Lorentz force on a fluid flow. The effect of varying such parameters as fluid properties, flow velocities, and the force magnitude could be visualized in a relatively short amount of time. Although various physical constants were variable, the effect of any changes were not easy to describe in terms of typical fluid dynamic parameters. In order to distinguish the effect of different parameters, it would be useful to solve the governing equations in a non-dimensional form.

The current work began with the development of a CFD code that solved the governing equations in non-dimensional form. This allows for a direct comparison of viscous, inertial, gravitational, and Lorentz forces. The Lorentz force term used in numerical simulations was derived using electrostatic principles. It was then expressed in

terms of the electrode diameter used in actual applications by performing finite element solutions of the electric potential. The CFD code developed was then used to study the effect of various force ratios.

A slot burner which was based on previous designs (Pattee and Peterson, 1993, Wolfard and Parker, 1949) was fabricated. It produced a smooth, laminar flame sheet which is ideal for studying the Lorentz mixing process. Alternate methods for introducing seed species were also tested. It was determined that the method of seeding the combustion gases used by Pattee and Peterson was more feasible for continuous operation. Experiments which could be used to determine the effectiveness of the Lorentz mixing process are surveyed as an outline of possible future work.

### Acknowledgments

The author would like to thank the National Science Foundation for its support of this research and Dr. H. A. Pattee for her mentoring and friendship. Also, many thanks go out to Drs. A. Stetz, P. Siemens, and J. Zaworski for the many hours of helpful discussion and review they gave.

## THEORETICAL DEVELOPMENT

The physical laws which govern the motion of fluids and the propagation of electromagnetic waves have been well established. The assumptions of constant fluid density, temperature, and viscosity and low electromagnetic oscillation frequency are used to describe the relevant governing equations from which a computer model is made. The solution of the governing equations is simplified by performing dimensional analysis which clarifies the physical meaning of each term in the governing equations. Finally, the physical laws are used to derive the force that arises due to the interactions of charged particles within the fluid. The force is expressed in a form which is general and can be further described based on the specific application at hand.

### Conservation Equations

The equations used to describe fluid flow are those of conservation of mass and momentum. For a viscous, incompressible fluid, these equations are (Nunn, 1989):

$$\frac{\partial u}{\partial x} + \frac{\partial v}{\partial y} = 0 \quad (1)$$

$$\frac{\partial u}{\partial t} + \frac{\partial(u^2)}{\partial x} + \frac{\partial(uv)}{\partial y} = -\frac{1}{\rho} \frac{\partial P}{\partial x} + \frac{\mu}{\rho} \left( \frac{\partial^2 u}{\partial x^2} + \frac{\partial^2 u}{\partial y^2} \right) + \frac{f_x}{\rho} \quad (2a)$$

$$\frac{\partial v}{\partial t} + \frac{\partial(uv)}{\partial x} + \frac{\partial(v^2)}{\partial y} = -\frac{1}{\rho} \frac{\partial P}{\partial y} + \frac{\mu}{\rho} \left( \frac{\partial^2 v}{\partial x^2} + \frac{\partial^2 v}{\partial y^2} \right) + \frac{f_y}{\rho} \quad (2b)$$

Complete modeling of Lorentz forces in combustion flames also requires an equation describing the conservation of energy. Appreciable Lorentz forces can be created in gases which have a very high electrical conductivities. The conductivity of a gas is a strong function of its temperature and can be increased by the introduction of a

seed species (Angrist, 1982). Since the seed species will only be present at elevated temperatures within the combustion zone, the conductivity of the flame will only be appreciable in this region. We may therefore localize the Lorentz force by defining a narrow region of the flow in which the seed species is present. This allows us to solve for the conservation of chemical species rather than the conservation of energy and to focus solely on the fluid dynamic interactions which are vital to the mixing process. For a binary mixture, this equation is (Incopera and De Witt, 1990):

$$\frac{\partial C_n}{\partial t} + \frac{\partial(uC_n)}{\partial x} + \frac{\partial(vC_n)}{\partial y} = D_{n \leftrightarrow n} \left( \frac{\partial^2 C_n}{\partial x^2} + \frac{\partial^2 C_n}{\partial y^2} \right) \quad (3)$$

The inclusion of electromagnetic effects requires the equations of electromagnetism to also be solved. These are known as Maxwell's equations (Lorrain, et al., 1988):

$$\nabla \cdot \mathbf{E} = \frac{q}{4\pi\epsilon_o} \quad (4)$$

$$\nabla \times \mathbf{E} = -\frac{\partial \mathbf{B}}{\partial t} \quad (5)$$

$$\nabla \cdot \mathbf{B} = 0 \quad (6)$$

$$(\nabla \times \mathbf{B}) = \mu_o \mathbf{J} + \mu_o \epsilon_o \frac{\partial \mathbf{E}}{\partial t} \quad (7)$$

We can neglect the time variations in the fields if the current density is the dominant term in the right-hand side of Eq. (7) (Pattee et. al., 1996). Substituting  $\sigma \mathbf{E}$  for  $\mathbf{J}$  and noting that the magnitude of the electric field can be expressed as a harmonic function, Eq. (7) becomes:

$$(\nabla \times \mathbf{B}) = \mu_o \sigma \sin(\omega t) \mathbf{E} + \omega \mu_o \epsilon_o \cos(\omega t) \mathbf{E} \quad (8)$$

Comparing the absolute magnitudes of the two terms on the right hand side of Eq. (8), it is clear that the current density will be the dominant term provided that:

$$\omega \ll \frac{\sigma}{\epsilon_0} \quad (9)$$

For a plasma with an electrical conductivity on the order of 100 mho/m,  $\sigma/\epsilon_0$  is on the order of  $10^{10}$  to  $10^{12}$  radians per second. This implies that the time variation in the fields may be neglected for oscillation frequencies below  $10^8$  Hz. This precludes the much more complex solution of the complete Maxwell equations.

Lorentz forces are the desired electromagnetic effect. A Lorentz force arises from the interaction of electric and magnetic fields with charged particles. When a fluid with an electric charge density  $\rho_q$  and current density  $\mathbf{J}$  flows through a region containing an electric field  $\mathbf{E}$  and a magnetic flux density  $\mathbf{B}$ , a force results (Lorrain et. al., 1988):

$$\mathbf{f} = \rho_q \mathbf{E} + \mathbf{J} \times \mathbf{B} \quad (10)$$

The first term on the right hand side represents an electrostatic component experienced by all charges irrespective of motion. The second term represents the dynamic component experienced by all moving charges in a region occupying a magnetic field. As mentioned previously, it is a reasonable approximation to use only the applied fields in Eq. (10) for low frequencies.

Again expressing the current density in terms of an applied current  $\sigma \mathbf{E}$  and an induced current  $\sigma \mathbf{V} \times \mathbf{B}$ , the Lorentz force may be expressed as:

$$\mathbf{f} = \rho_q \mathbf{E} + [\sigma \mathbf{E} + \sigma (\mathbf{V} \times \mathbf{B})] \times \mathbf{B} \quad (11)$$

In typical applications with applied electric fields, the applied current will be several orders of magnitude greater than the induced current. Under these conditions, Eq. (11) may be

simplified to:

$$\mathbf{f} = \rho_q \mathbf{E} + (\sigma \mathbf{E} \times \mathbf{B}) \quad (12)$$

From the geometry of Fig. 3.6, the electrostatic component of the force is perpendicular to the computational plane and will be neglected. Note also that if the applied magnetic field is aligned parallel to the y-axis, then on the computational plane Eq. (12) becomes:

$$\mathbf{f} = \sigma \mathbf{E} \mathbf{B} \quad (13)$$

Unlike a gravitational force, typically a constant that is considered either present or absent, the Lorentz force requires a more elaborate description to account for spatial and temporal variations in the fields.

### Dimensional Analysis

Dimensional analysis is used to ensure dimensional homogeneity, to ensure geometric and kinematic similarity, and to uncover the physical meaning of governing equations. The relevant variables are the fluid velocity, fluid properties, pressure, and electromagnetic field parameters. To employ the Buckingham Pi method (Welty et al, 1984), it is proposed that the fluid velocity is a function of the other variables. Selecting a core group of  $(\rho, \sigma, z_o, \omega)$ , the following dimensionless groups can be readily formed:

$$\text{Group 1:} \quad (\rho, \sigma, z_o, \omega) + u \Rightarrow \left[ \frac{u}{\omega \cdot z_o} \right] \equiv u^+ \quad (14a)$$

$$\text{Group 2:} \quad (\rho, \sigma, z_o, \omega) + \mu \Rightarrow \left[ \frac{\mu}{\rho \cdot z_o^2 \cdot \omega} \right] \equiv \mu^+ \quad (14b)$$

$$\text{Group 3:} \quad (\rho, \sigma, z_o, \omega) + P \Rightarrow \left[ \frac{P}{\rho \cdot z_o^2 \cdot \omega^2} \right] \equiv P^+ \quad (14c)$$

$$\text{Group 4: } (\rho, \sigma, z_o, \omega) + \Delta V \Rightarrow \sqrt{\frac{\sigma \cdot (\Delta V)^2}{\rho \cdot z_o^4 \cdot \omega^3}} \equiv V^+ \quad (14d)$$

$$\text{Group 5: } (\rho, \sigma, z_o, \omega) + B \Rightarrow \sqrt{\frac{\sigma \cdot B^2}{\rho \cdot \omega}} \equiv B^+ \quad (14e)$$

$$\text{Group 6: } (\rho, \sigma, z_o, \omega) + x \Rightarrow \left[ \frac{x}{z_o} \right] \equiv x^+ \quad (14f)$$

$$\text{Group 7: } (\rho, \sigma, z_o, \omega) + t \Rightarrow [\omega \cdot t] \equiv t^+ \quad (14g)$$

Similar to groups 1 and 6, two groups can be formed for the y-components of velocity and position, respectively. In terms of the inlet concentration of seed species in the combustion zone,  $C_o$ , a non-dimensional species concentration is defined as:

$$X_n \equiv \left[ \frac{C_n}{C_o} \right] \quad (15)$$

It is useful to define a reference velocity based on the frequency of the Lorentz force and the distance from the tip of the electrode to the equipotential plane (Pattee, et al 1996):

$$U_{ref} = \omega \cdot z_o \quad (16)$$

Dropping the + superscripts and substituting Eqs. (14)-(16) into Eqs. (1)-(3), the following non-dimensional forms of the conservation equations can be obtained:

$$\frac{\partial u}{\partial x} + \frac{\partial v}{\partial y} = 0 \quad (17)$$

$$\frac{\partial u}{\partial t} + \frac{\partial(u^2)}{\partial x} + \frac{\partial(u \cdot v)}{\partial y} = - \left[ \frac{\Delta P}{\rho \cdot U_{ref}^2} \right] \frac{\partial P}{\partial x} + \left[ \frac{\mu}{\rho \cdot U_{ref} \cdot z_o} \right] \left( \frac{\partial^2 u}{\partial x^2} + \frac{\partial^2 u}{\partial y^2} \right) + \left[ \frac{z_o \cdot f_x}{\rho \cdot U_{ref}^2} \right] \quad (18a)$$

$$\frac{\partial v}{\partial t} + \frac{\partial(u \cdot v)}{\partial x} + \frac{\partial(v^2)}{\partial y} = - \left[ \frac{\Delta P}{\rho \cdot U_{ref}^2} \right] \frac{\partial P}{\partial y} + \left[ \frac{\mu}{\rho \cdot U_{ref} \cdot z_o} \right] \left( \frac{\partial^2 v}{\partial x^2} + \frac{\partial^2 v}{\partial y^2} \right) + \left[ \frac{z_o \cdot f_y}{\rho \cdot U_{ref}^2} \right] \quad (18b)$$

$$\frac{\partial X_n}{\partial t} + \frac{\partial(u \cdot X_n)}{\partial x} + \frac{\partial(v \cdot X_n)}{\partial y} = \left[ \frac{D_{n \leftrightarrow n}}{\omega \cdot C_o} \right] \left( \frac{\partial^2 X_n}{\partial x^2} + \frac{\partial^2 X_n}{\partial y^2} \right) \quad (19)$$

The bracketed terms of Eq. (18) represent ratios of forces. They are the Euler number, Reynolds number, and another term,  $\Pi_1$ . The Euler and Reynolds numbers represent the ratios of pressure and viscous forces to inertial forces, respectively. This other term represents the ratio of body forces to inertial forces. For the special case of gravity, this term is known as the Froude number. The Froude number represents the ratio of inertial to gravitational forces. For the geometry chosen, the x-component of force is the Lorentz force and this number represents the ratio of Lorentz forces to inertial forces.

$$\begin{aligned} Eu_\omega &= \frac{\Delta P}{\rho \cdot U_{ref}^2} & Re_\omega &= \frac{\rho \cdot U_{ref} \cdot z_o}{\mu} \\ Fr_\omega &= \frac{U_{ref}^2}{g_o \cdot z_o} & \Pi_1 &= \frac{z_o \cdot f_x}{\rho \cdot U_{ref}^2} \end{aligned} \quad (20)$$

Substituting Eqs. (20) into Eqs. (18), yields the final form of the non-dimensional x and y momentum equations:

$$\frac{\partial u}{\partial t} + \frac{\partial(u^2)}{\partial x} + \frac{\partial(u \cdot v)}{\partial y} = -Eu \frac{\partial P}{\partial x} + \left[ \frac{1}{Re} \right] \left( \frac{\partial^2 u}{\partial x^2} + \frac{\partial^2 u}{\partial y^2} \right) + \Pi_1 \quad (21a)$$

$$\frac{\partial v}{\partial t} + \frac{\partial(u \cdot v)}{\partial x} + \frac{\partial(v^2)}{\partial y} = -Eu \frac{\partial P}{\partial y} + \left[ \frac{1}{Re} \right] \left( \frac{\partial^2 v}{\partial x^2} + \frac{\partial^2 v}{\partial y^2} \right) + \left[ \frac{1}{Fr} \right] \quad (21b)$$

Eqs. (21), along with Eqs. (17) and (19), are the final forms of the governing equations which are solved numerically. For all computations the Froude number is taken to be zero. This reduces the number of dimensionless numbers of interest to three and highlights the effects of the parameter  $\Pi_1$ .

The term  $\Pi_1$  is different from previous non-dimensional parameters used to describe electromagnetic effects (Cramer and Pal, 1973):

$$\text{Magnetic Pressure Number, } R_H = \frac{\mu_o^{-1} B^2}{\rho U^2} \equiv \frac{\text{Magnetic Pressure}}{\text{Dynamic Pressure}}$$

$$\text{Hartman Number, } R_h = BL \sqrt{\frac{\sigma}{\mu}} \equiv \frac{\text{Magnetic Force}}{\text{Viscous Force}} \quad (22)$$

$$\text{Magnetic Number, } R_m = B \left( \frac{\sigma L}{\rho U} \right) \equiv \frac{\text{Magnetic Force}}{\text{Inertial Force}}$$

The primary difference between the dimensionless numbers of Eqs. (20) and (22) is the use of the unique reference velocity,  $\omega z_o$ . The term  $\Pi_1$  most closely resembles the Magnetic Number, the major difference being that the Lorentz force is a function of both the electric and magnetic fields, rather than a magnetic field alone.

## NUMERICAL IMPLEMENTATION

The first step in investigating the effect of an externally applied Lorentz force on flow behavior is to develop an adequate description of the force which captures the spatial and temporal variations that distinguish it from traditional body forces. After this is accomplished, the formulation for the force is implemented into a computer model. Flow simulations are performed to investigate the effect of varying different parameters. The numerical solution techniques used in CFD depend greatly on the type of flow being modeled. The computer model developed here is for an internal, incompressible, isothermal, viscous flow of a binary mixture. The SIMPLE method, a well-known solution algorithm, is used with up winding on a staggered grid to solve for the flow field variables. Fick's law is used to compute the concentrations of the mixture.

### Description of the Lorentz Force

The most common physical means of introducing a Lorentz force to a fluid is by applying a voltage across electrodes that are positioned in or near the flow stream and applying a properly oriented magnetic field. Neglecting variations in the electrical conductivity of the fluid, the resulting electric field will primarily depend on the charge distribution on the electrode surfaces. It would be useful to relate the electric field to physical parameters such as electrode diameter, applied voltage, and physical geometry. To accomplish this, an analytical expression for the electric field is derived. This expression is then correlated with the results of finite element (FE) solutions. The resultant correlation can then be used to estimate the value of electric field for a given electrode configuration (specified electrode diameter and electrode separation) without requiring the solution of the Maxwell equations.

For increased values of the applied voltage, there will be an increased surface charge density near the tips of the electrodes. Since the charge density is greatest near the tips of the electrodes, the analysis is simplified by approximating the tips of the electrodes as uniformly charged spheres. From Coulomb's Law of electrostatics, the potential field for a single charged sphere is (Lorrain et. al., 1988):

$$V(\mathbf{r}) = \frac{1}{4\pi\epsilon_0} \cdot \frac{q}{|\mathbf{r} - \mathbf{r}_0|} \quad (23)$$

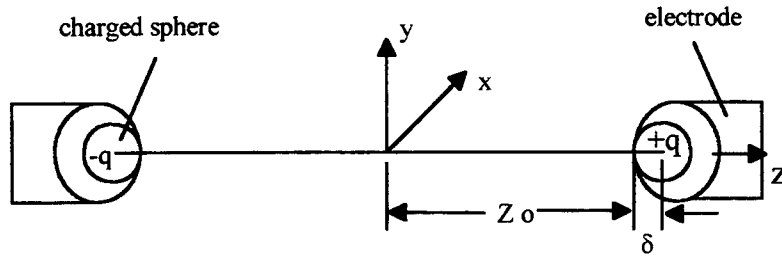


Figure 3.1 Replace electrodes with ideal charged spheres

Idealizing the electrodes as small charged spheres of radius  $\delta$ , carrying charges of  $+q$  and  $-q$ , the total scalar potential field is found directly by applying the principle of superposition to Eq. (23). If each sphere is centered on the  $z$ -axis a distance  $z_0$  from the origin of a right-handed coordinate system, as depicted in Figure 3.1, the potential field is:

$$V(x, y, z) = \frac{q}{4\pi\epsilon_0} \cdot \left[ \frac{1}{\sqrt{x^2 + y^2 + (z - z_0)^2}} - \frac{1}{\sqrt{x^2 + y^2 + (z + z_0)^2}} \right] \quad (24)$$

The electric field is readily obtained by taking the gradient of Eq. (24):

$$\mathbf{E}(x, y, z) = \frac{q}{4\pi\epsilon_0} \cdot \left\{ \begin{array}{l} \left[ \frac{x}{(x^2+y^2+(z+z_0)^2)^{1.5}} - \frac{x}{(x^2+y^2+(z-z_0)^2)^{1.5}} \right] \mathbf{e}_x \\ + \left[ \frac{y}{(x^2+y^2+(z+z_0)^2)^{1.5}} - \frac{y}{(x^2+y^2+(z-z_0)^2)^{1.5}} \right] \mathbf{e}_y \\ + \left[ \frac{(z+z_0)}{(x^2+y^2+(z+z_0)^2)^{1.5}} - \frac{(z-z_0)}{(x^2+y^2+(z-z_0)^2)^{1.5}} \right] \mathbf{e}_z \end{array} \right\} \quad (25)$$

By inspection, this electric field satisfies Eq. (5) for the condition of a constant magnetic field. Eqs. (24) and (25) cannot be evaluated because the charge of the idealized sphere is not yet known. However, the magnitude of the charge can be obtained by taking the difference between the values of the scalar potential at the surfaces of each sphere and equating it to the applied voltage:

$$\Delta V = V(0, 0, z_0 - \delta) - V(0, 0, -z_0 + \delta) \quad (26)$$

Evaluating Eq. (26) with Eq. (24) and solving for the quantity of charge,

$$q = \Delta V \cdot 4\pi\epsilon_0 \cdot \left[ \frac{\delta(2z_0 - \delta)}{4(z_0 - \delta)} \right] \quad (27)$$

The electric field can now be calculated by substituting Eq. (27) into Eq. (25). If we focus our attention on the equipotential (x,y) plane, the electric field is reduced to a single component parallel to the z-axis:

$$\mathbf{E}(x, y, 0) = \left[ \frac{z_0 \delta (2z_0 - \delta)}{(x^2 + y^2 + z_0^2)^{1.5}} \right] \cdot \left[ \frac{\Delta V}{2(z_0 - \delta)} \right] \mathbf{e}_z \quad (28)$$

The right hand side of Eq. (28) is the familiar expression for the electric field between two infinite, flat, parallel plates separated by a distance of  $2(z_0 - \delta)$  (Lorrain et. al., 1988), multiplied by a spatial scaling factor. Eq. (28) is plotted in Figure 3.2 for a fixed distance between spheres of 2 cm and varying values of  $\delta$ . As is expected, the parallel-plate solution is approached as  $\delta$  increases.

The above expressions for the scalar potential and the electric field are valid for static conditions with the assumption of a uniform, glow discharge. The model is not valid for an arc discharge. If a variable, rather than a constant, voltage is applied across the electrodes, the fields will have some variations in the regions near the electrode surfaces due to varying charge distributions. As mentioned previously, the induced fields may be neglected for low frequencies.

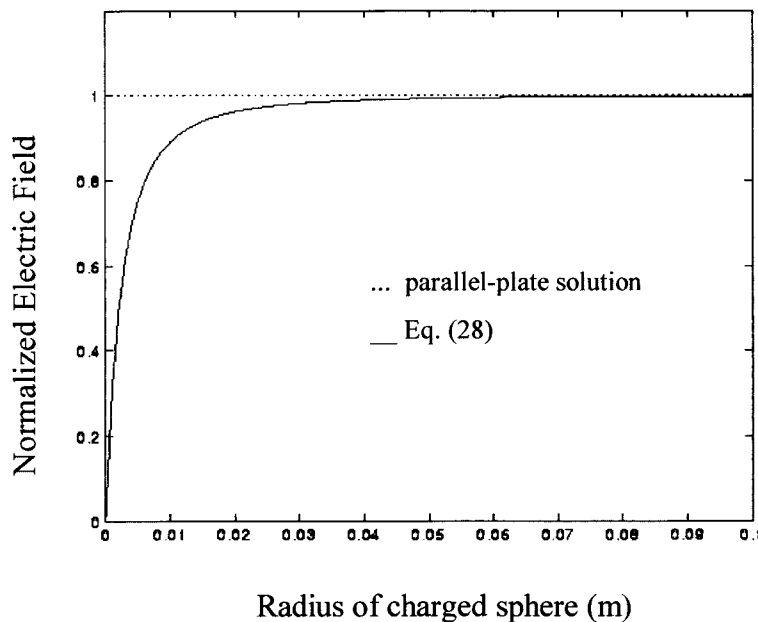


Figure 3.2 Comparison of electric field for an infinite parallel-plate capacitor with Eq. (28).

Eq. (22) provides a simple way to estimate the electric field, and thus the Lorentz force, without solving the Maxwell equations. The only unknown quantity is the radius of the charged sphere,  $\delta$ . In order to incorporate Eq. (28) into Eq. (21a), a functional relationship between the diameters of the idealized spheres and actual electrodes is needed. Finite element (FE) solutions of the scalar potential and electric field were performed on the equipotential plane described by Eq. (28) for a specified distance between electrodes of 2 cm and varying electrode diameters.

The FE solutions were performed for the scalar potential using the program UCODE3 (Akay, 1990) with four-sided elements. The program required an input file which defined the FE mesh, the equation being solved, and the boundary conditions. For a static electric field, the scalar potential obeys Laplace's equation:

$$\nabla^2 V = 0 \quad (29)$$

Since the scalar potential and the electric fields are symmetric about the z-axis, solution of Laplace's equation reduces to a 2-D problem. Symmetry boundary conditions were used between electrodes along the z-axis. The elements defining the electrodes were defined to be held at fixed potentials and the side boundaries were defined to have constant derivatives. The potential along the upper boundary was set to zero - a condition which is true only at an infinite distance away from the electrodes. The use of this boundary condition required an extended grid in order to prevent biasing of the solution.

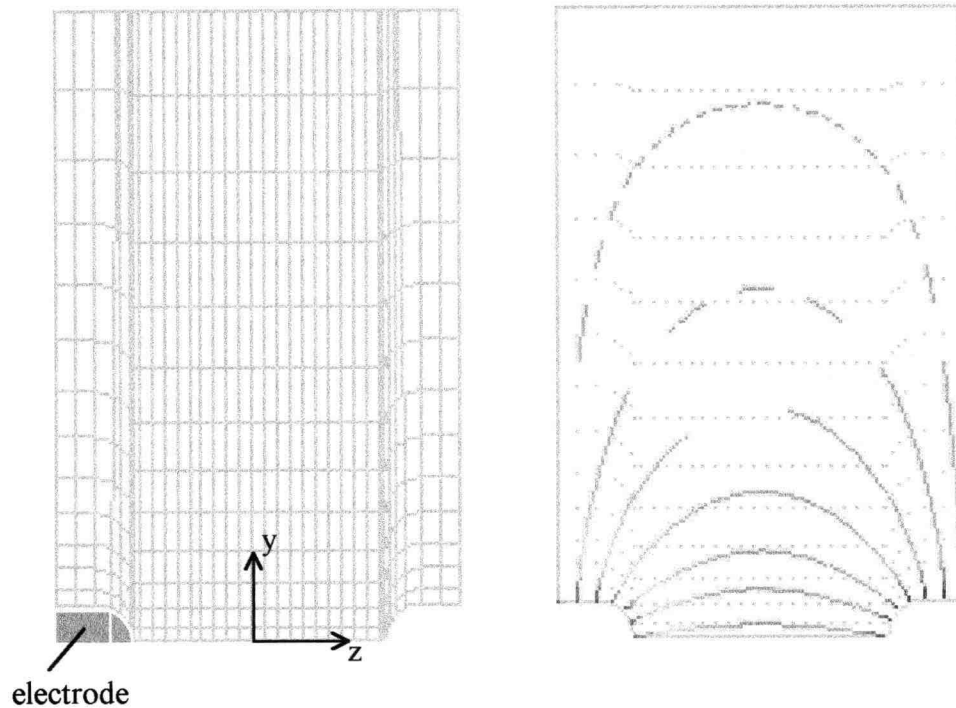


Figure 3.3 FE mesh and lines of constant electric field.

Electrodes with diameters ranging from 2 mm to 8 mm were used. After performing several solutions, it was determined that the inclusion of electrode lengths of more than two diameters had a negligible effect on the solution in the region of interest. Physically this is appropriate since almost all of the charge will collect near the tips of the electrodes. Values of the electric field were computed by the program as the gradient of the solution over the FE mesh and written to an output file. Solutions were performed for electrodes with both round and pointed tips and a fixed separation of 2 cm. The FE mesh and solution are shown in Figure 3.3. The dark shading near the tips represents regions of high and low potential and the electric field contours represent a stronger field where they are more dense.

The solutions of the electric field were plotted against Eq. (28) and the values of  $\delta$  were adjusted to give the best fit for each electrode diameter. This is illustrated in Figure 3.4 for the case of 3 mm electrodes.

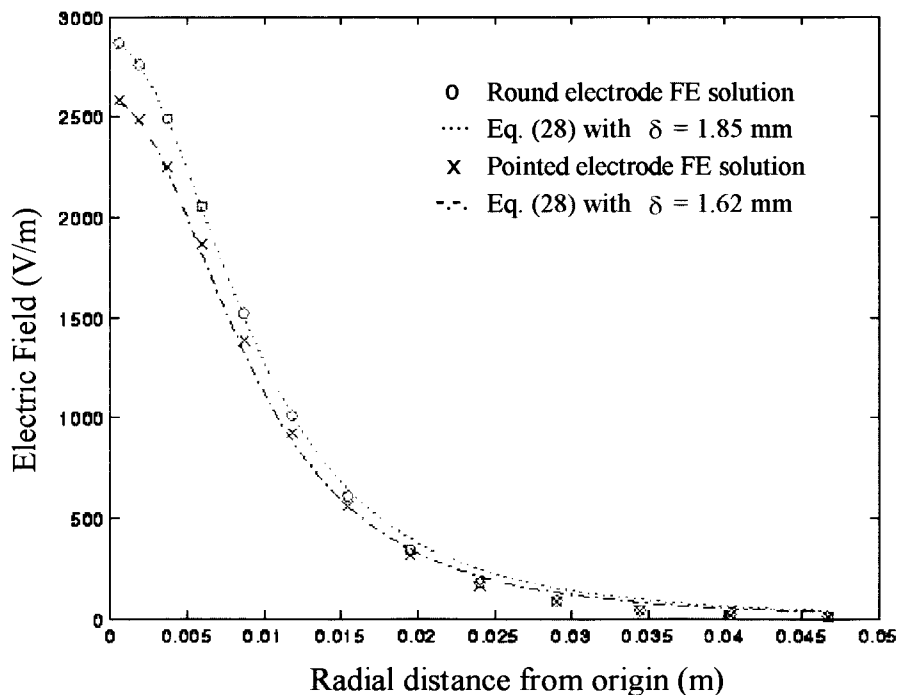


Figure 3.4 Comparison of Eq. (28) with 3 mm FE solution.

In actual applications, electrodes are often made to have sharply pointed tips. This is done in an effort to collect the largest amount of charge which increases the field strength and promotes conduction through the fluid. Over time, the electrode surfaces become worn and must be re-sharpened. Considering both round and pointed electrodes,

the fitted values of  $\delta$  were then plotted against the electrode diameters to obtain a functional relationship. The results are shown graphically in Figure 3.5.

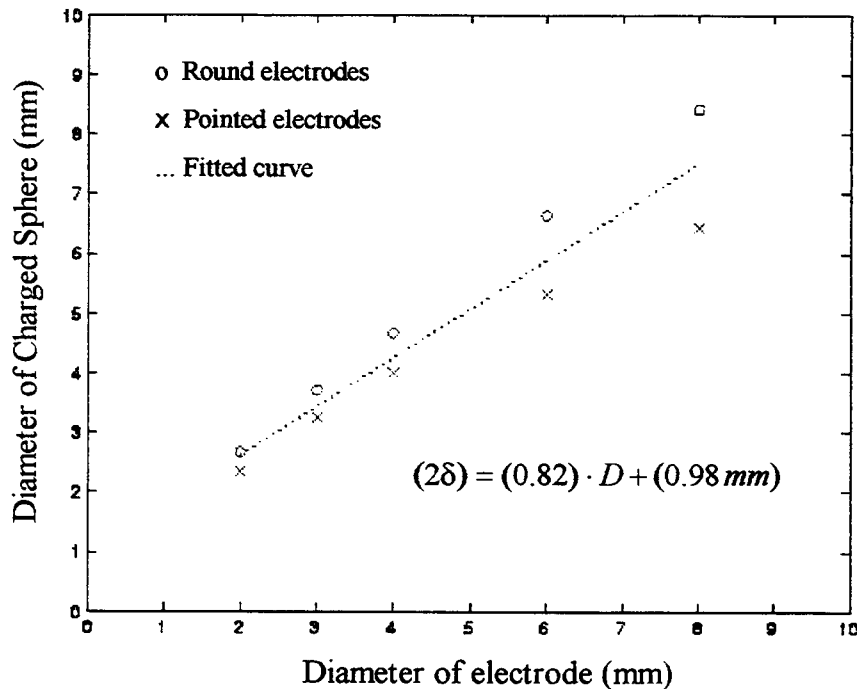


Figure 3.5 Correlation of ideal sphere diameter with electrode diameter used in FE solutions for a fixed distance between electrodes of 2 cm.

The correlation of Figure 3.5 and Eq. (28) was then used to compute the magnitude of the Lorentz force over the computational plane. This calculation was done and the resulting values were stored in an input file used for the CFD simulations. In general, this procedure can be done in two steps. The first step is to create a suitable FE mesh and compute the values of the electric field on the equipotential plane. The second step is to correlate the electrode diameters to  $\delta$  by comparing the results of  $\delta$  with Eq. (28)

to the FE solution. This allows obtaining the electric field distribution for any pair of electrodes separated by a fixed distance.

### Computational Domain

The region of interest is defined according to the position of the electrodes used to induce Lorentz forces and the flame sheet these forces act upon. The computational plane coincides with the equipotential plane located midway between the electrodes. The flame sheet lies parallel to the dashed line of Fig. 3.6.

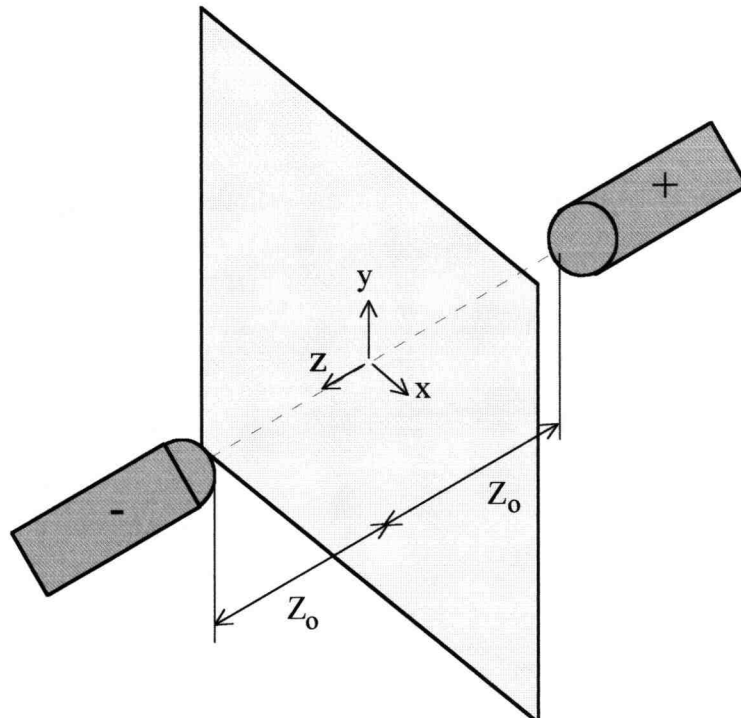


Figure 3.6 Computational domain defined as equipotential plane between electrodes.

A staggered grid was used for the solution of the non-dimensional momentum equation, Eqs. (21). The use of a staggered grid facilitates the use of up winding schemes for computing flux terms and numerical derivatives. Rather than defining the values of  $u$ ,  $v$ , and  $P$  at coincident grid points (Fig. 3.7a), use was made of continuity and momentum cells. Continuity cells are centered about points where scalar quantities (pressure, divergence, concentration, etc.) are defined (Fig. 3.7b). Momentum cells are centered about points where the components of the velocity vector are defined. These two types of cells are offset by a half node in both the  $x$  and  $y$  directions. Figure 3.8 shows how continuity and momentum cells are arranged.

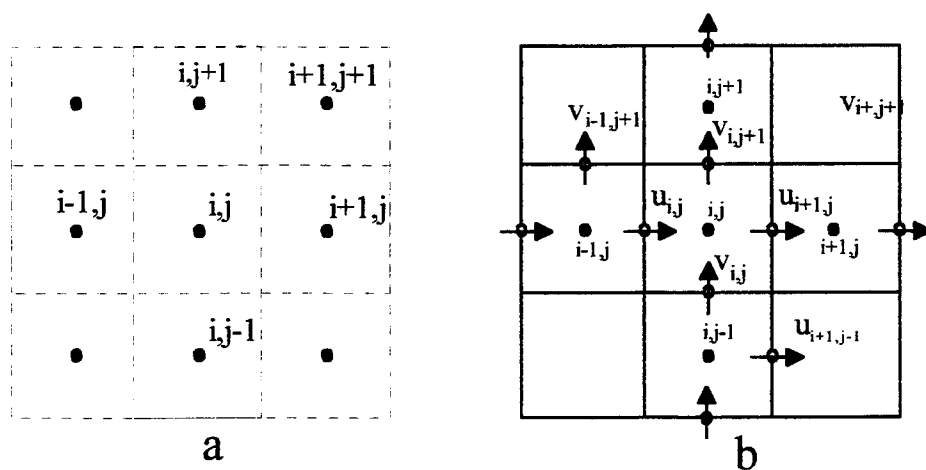


Figure 3.7 (a) Normal grid with all variables defined at the same  $(i, j)$  grid points and (b) Staggered grid with scalar variables defined at  $(i, j)$  grid points and vector components defined on cell faces centered about  $(i, j)$  grid points.

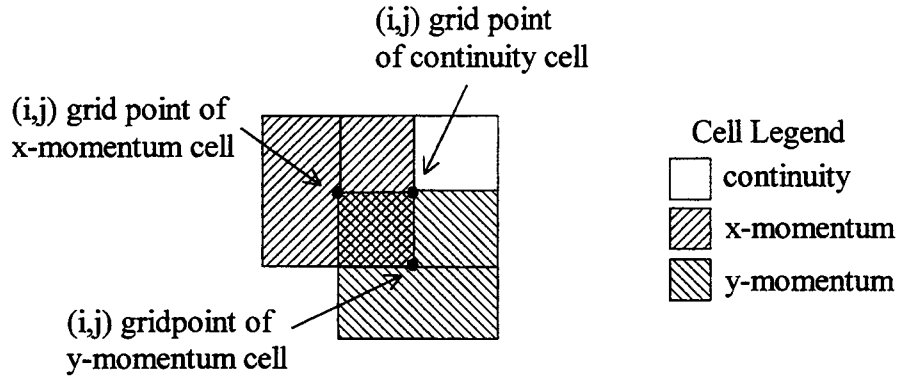


Figure 3.8 Staggering of continuity and momentum cells.

The advantage of the staggered grid becomes readily apparent when computing scalar quantities such as divergence. A centered difference approximation can be used to calculate the velocity gradients over the entire flow field. For example, the discrete divergence of velocity at the point  $(i,j)$ , from Figure 3.7b, is:

$$(\nabla \cdot \mathbf{v})_{ij} = \frac{u_{ij} - u_{i-1j}}{\Delta x} + \frac{v_{ij} - v_{ij-1}}{\Delta y} \quad (30)$$

Computing this quantity for the grid of Figure 3.7a would require using special difference approximations along the boundaries. This is because centered difference expressions require  $(i,j \pm 1)$  terms to compute their value.

The up winding method used to calculate the fluxing terms of Eqs. (19) and (21) also takes advantage of the staggered grid. For this method, the fluxing velocity components are taken as the average values of the velocity on the faces of the momentum cell. For a positive fluxing velocity component, the velocity component in the center of the previous cell is used as the fluxed component. For a negative fluxing component, the

velocity component in the center of the next cell is used as the fluxed component. This is illustrated in Figure 3.9 for the terms of the X-momentum equation. The values used in the Y-momentum equation are obtained similarly.

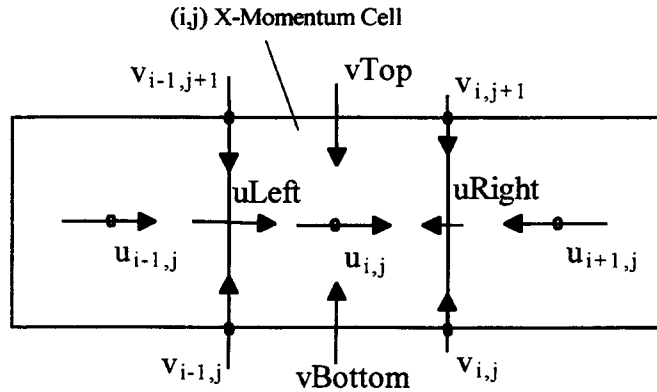


Figure 3.9 Velocities used to compute flux terms of X-momentum equation.

For example, the fluxing quantities for the x-momentum equation are computed as:

$$uu_{Left} = \frac{1}{2} \cdot [(u_{Left} + \text{abs}(u_{Left})) \cdot u_{i-1,j} + (u_{Left} - \text{abs}(u_{Left})) \cdot u_{i,j}]$$

$$uu_{Right} = \frac{1}{2} \cdot [(u_{Right} + \text{abs}(u_{Right})) \cdot u_{i,j} + (u_{Right} - \text{abs}(u_{Right})) \cdot u_{i+1,j}]$$

(31a)

$$uv_{Top} = \frac{1}{2} \cdot [(v_{Top} + \text{abs}(v_{Top})) \cdot u_{i,j} + (v_{Top} - \text{abs}(v_{Top})) \cdot u_{i,j+1}]$$

$$uv_{Bottom} = \frac{1}{2} \cdot [(v_{Bottom} + \text{abs}(v_{Bottom})) \cdot u_{i,j-1} + (v_{Bottom} - \text{abs}(v_{Bottom})) \cdot u_{i,j}]$$

From which the fluxing derivatives are taken as:

$$\frac{\partial(uu)}{\partial x} \approx \frac{uu_{\text{Right}} - uu_{\text{Left}}}{\Delta x}$$

$$\frac{\partial(uv)}{\partial y} \approx \frac{uv_{\text{Top}} - uv_{\text{Bottom}}}{\Delta y}$$
(31b)

A similar procedure is used for the y-momentum equation. Notice that for the cross terms, (uv) and (vu), averaged values of the fluxed quantity are used because they best represent the values of the momentum cell.

### Fluid Flow

The Semi-Implicit Method for Pressure-Linked Equations (SIMPLE) was used to solve Eqs. (21) for the flow field variables  $u$ ,  $v$ , and  $P$  (Anderson, 1995). "Semi-Implicit" stems from a combination of explicit and implicit solution techniques. It is logical and straightforward when solving the momentum equations numerically to march the velocity components using an explicit solution method. The difficulty that arises is ensuring mass conservation. An equation derived from mass conservation can be solved implicitly which not only yields a correction for the explicit velocity prediction, but also solves for the pressure.

The method begins by assuming that the values of the pressure field are known. The next step is to predict values of the velocity components based on the assumed pressure field using the purely explicit form:

$$u_{ij}^{t+\Delta t} = u_{ij}^t + \Delta t \cdot \left[ \frac{1}{Re_\omega} \left( \frac{\partial^2 u}{\partial x^2} + \frac{\partial^2 u}{\partial y^2} \right)_{ij}^t + \Pi_1 \sin(t) \right] - \Delta t \cdot Eu_\omega \left( \frac{\partial P}{\partial x} \right)_{ij}^t \quad (32a)$$

$$v_{ij}^{t+\Delta t} = v_{ij}^t + \Delta t \cdot \left[ \frac{1}{Re_\omega} \left( \frac{\partial^2 v}{\partial x^2} + \frac{\partial^2 v}{\partial y^2} \right)_{ij}^t + Fr_\omega \right] - \Delta t \cdot Eu_\omega \left( \frac{\partial P}{\partial y} \right)_{ij}^t \quad (32b)$$

Since these are only predicted values and not the actual values of the velocity components, substitution of Eqs. (32) into the continuity equation, Eq. (17), will not produce the desired value of zero. However, if we were to adjust the predicted velocity values the right amount, then the new, corrected values would in fact satisfy Eq. (17). That is,

$$\frac{\partial(u+u^*)}{\partial x} + \frac{\partial(v+v^*)}{\partial y} = 0 \quad (33)$$

If we can find the values of  $u^*$  and  $v^*$ , then we can satisfy Eq. (33). This can be done by making the rationalization that if we had used the correct value of pressure ( $P+P^*$ ) in Eqs. (32), then we could have satisfied Eq. (17). Defining the pressure correction in terms of a solution variable,  $\beta$ , as  $P^* = \beta/\Delta t$  and including it into Eqs. (32),

$$u_{ij}^{t+\Delta t} = u_{ij}^t + \Delta t \cdot \left[ \frac{1}{Re_\omega} \left( \frac{\partial^2 u}{\partial x^2} + \frac{\partial^2 u}{\partial y^2} \right)_{ij}^t + \Pi_1 \sin(t) \right] - \Delta t \cdot Eu_\omega \left[ \frac{\partial \left( P + \frac{\beta}{\Delta t} \right)}{\partial x} \right]_{ij}^t \quad (34a)$$

$$v_{ij}^{t+\Delta t} = v_{ij}^t + \Delta t \cdot \left[ \frac{1}{Re_\omega} \left( \frac{\partial^2 v}{\partial x^2} + \frac{\partial^2 v}{\partial y^2} \right)_{ij}^t + Fr_\omega \right] - \Delta t \cdot Eu_\omega \left[ \frac{\partial \left( P + \frac{\beta}{\Delta t} \right)}{\partial y} \right]_{ij}^t \quad (34b)$$

Eqs. (34) are the corrected velocities that are to satisfy continuity. Notice the difference between Eqs. (34) and Eqs. (32) are the velocity corrections:

$$u^* = -Eu_\omega \cdot \frac{\partial \beta}{\partial x} \quad (35a)$$

$$v^* = -Eu_\omega \cdot \frac{\partial \beta}{\partial y} \quad (35b)$$

An equation for the solution variable is obtained by substituting Eqs. (35) into Eq. (33):

$$\frac{\partial^2 \beta}{\partial x^2} + \frac{\partial^2 \beta}{\partial y^2} = \frac{(\nabla \cdot \mathbf{v})^t}{Eu_\omega} \quad (36)$$

This is Poisson's equation for  $\beta$ , which is an elliptic equation and can be solved implicitly using a Thomas algorithm. In the computer program generated here, the  $\beta$  equation is solved semi-implicitly using a point-to-point method. The  $t$  superscript on the divergence notes that this value is to be calculated with the predicted value of the velocity at the current time step.

Traditionally, the SIMPLE method has been used to obtain steady-state solutions of the velocity and pressure fields. The general procedure by which this is done may be expanded to obtain the solution of transient flow behavior. This is done by iterating on the divergence within each time step until it is below a specified tolerance.

### Species Diffusion

The magnitude of the Lorentz force given by Eq. (28) is directly proportional to the conductivity of the fluid. The conductivity of most gases is very low at combustion temperatures and there are relatively few ionized species present. One method of overcoming this is to introduce a seed species, such as an alkali metal. Conductivities of seeded flames are several orders of magnitude greater than those of unseeded flames. Since the seed species will only be present at elevated temperatures over a narrow region defined by the combustion zone. Flow simulations were done with an inlet species concentration of 1.0 over the first three nodes above the midplane in the  $y$ -direction and zero at all other nodes. The concentration was then able to diffuse out into the bulk of the flow. This had the effect of localizing the Lorentz force to a region resembling the combustion zone.

The non-dimensional diffusion equation was solved purely explicitly by writing it in the following form:

$$X_{ij}^{t+\delta t} = X_{ij}^t + \delta t \cdot \left\{ \frac{D_{n \leftrightarrow n}}{\omega \cdot C_o} \cdot \left( \frac{\partial^2 X}{\partial x^2} + \frac{\partial^2 X}{\partial y^2} \right)_{ij}^t - u_{ij}^{t_o} \left( \frac{\partial X}{\partial x} \right)_{ij}^t - v_{ij}^{t_o} \left( \frac{\partial X}{\partial y} \right)_{ij}^t \right\} \quad (37)$$

The time step used to solve the diffusion equation,  $\delta t$ , was smaller than the time step used to solve for the flow field variables,  $\Delta t$ . Thus, for each time step of the flow field solution, the values of the species concentration were progressed a number of smaller time steps. This assumes that the values of the flow field variables do not change appreciably between the times  $t_o$  and  $t_o + \Delta t$ .

### Turbulence

The rate at which species diffusion takes place is limited by molecular diffusion. The aim of applying a Lorentz force to the flow is to increase the mixing, to induce turbulence in the flow field. A turbulent diffusion coefficient was calculated using a Baldwin-Lomax turbulence model (Baldwin and Lomax, 1978). This model uses the local vorticity to determine turbulent coefficients. As with most turbulence models, several empirical constants are used which depend on the type of flow being considered. A turbulent viscosity is defined over two regions:

$$\mu_t = \left\{ \begin{array}{ll} (\mu_t)_{inner} & y \leq y_{crossover} \\ (\mu_t)_{outer} & y \geq y_{crossover} \end{array} \right\} \quad (38a)$$

In this expression,  $y$  is the distance from the edge boundary and  $y_{crossover}$  is defined as the value of  $y$  where  $(\mu_t)_{outer}$  becomes greater than  $(\mu_t)_{inner}$ . The inner and outer viscosities are defined by the following relations:

$$\begin{aligned}
(\mu_t)_{inner} &= \rho \cdot l^2 \cdot |\omega| \\
(\mu_t)_{outer} &= K \cdot C_{cp} \cdot F_{wake} \cdot K_{kleb}
\end{aligned}
\tag{38b}$$

The definition of the inner viscosity incorporates both the distance to the wall boundary and a vorticity because it is expected to reflect the value of the viscosity within a boundary layer. The outer viscosity uses only a vorticity because it is far from any wall boundaries and well outside of the boundary layer.

Various values for the constants  $C_{cp}$  and  $C_{kleb}$  have been used. The numbers used depend on which flow regime is being modeled. In the present work, the suggested values for incompressible flow of  $C_{cp}=1.2$  and  $C_{kleb}=0.65$  are used (He and Walker, 1995). In this model,  $K=0.0168$ ,  $A^+=26.0$ ,  $k$  is the thermal conductivity, and the other constants are defined as:

$$\begin{aligned}
F(y) &\equiv y|\omega| \left[ 1 - \exp\left(-\frac{y^+}{A^+}\right) \right] \\
l &\equiv ky \left[ 1 - \exp\left(-\frac{y^+}{A^+}\right) \right] \\
F_{wake} &\equiv \text{minimum of } (X_{max} \cdot F_{max}) \text{ and } \left( \frac{C_{wake} Y_{max} |\mathbf{v}|^2}{F_{max}} \right) \\
y^+ &\equiv \frac{\sqrt{\rho_w \tau_w y}}{\mu_w} \\
Y_{max} &\equiv y \text{ where } F(y) \text{ has its maximum} \\
|\omega| &\equiv \sqrt{\left( \frac{\partial u}{\partial y} - \frac{\partial v}{\partial x} \right)^2} \\
|\mathbf{v}|^2 &\equiv \mathbf{u}^2 + \mathbf{v}^2 \\
F_{kleb} &= \left[ 1 + 5.5 \left( \frac{C_{kleb} \cdot y}{Y_{max}} \right)^6 \right]^{-1}
\end{aligned}
\tag{38c}$$

Using the Prandtl and Lewis numbers, the turbulent thermal conductivity and diffusion coefficient can be obtained from the above relations. The apparent viscosity and diffusivity are then taken as the sum of the laminar and turbulent values.

$$k_t = \frac{\mu_t \cdot c_p}{Pr} \quad \text{and} \quad D_t = \frac{k_t \cdot Le}{\rho \cdot c_p}
\tag{39}$$

The turbulent viscosity has a value nearly equal to the laminar viscosity, and is greatest near the wall boundaries. Similarly, the turbulent part of the apparent diffusion coefficient is nearly equal to the laminar part. From Eqs. (39), the contours of Figures 3.10 and 3.11 show qualitatively the increase of both turbulent coefficients.

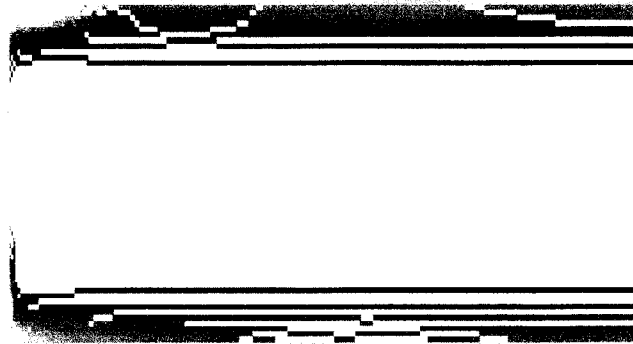


Figure 3.10 Contours of turbulent viscosity with a maximum value of  $9.1e-4$  occurring nearest the channel walls.

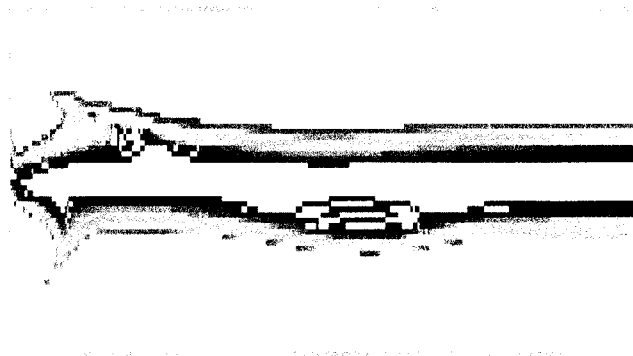


Figure 3.11 Contours of turbulent viscosity within the channel. Maximum value shown of  $1.0e-6$  occurs nearest the channel walls.

## NUMERICAL RESULTS

A numerical solution's ability to model the governing equations must be evaluated before its results can be used to make accurate statements regarding the outcome of any simulations. Whenever possible, the first step in evaluating the suitability of a numerical solution is to compare its results to exact solutions. Unfortunately, exact solutions are not always known. Under such circumstances, it is useful to compare a simplified model to the solution of the correspondingly simplified governing equations, which may be known. This is the present case. There are no exact solutions for flow subjected to Lorentz forces so the model is compared to the exact solution for the flow between two infinite flat plates, also known as Poiseuille flow. Numerical results are then obtained for more complex flows. The accuracy of these results is estimated by monitoring how well the solution obeys the laws of mass conservation. The results of flow simulations are used to form a factorial design of experiments from which insight into the significant flow parameters can be drawn.

### Code Validation

The partial differential form of the momentum equations makes exact solutions difficult, if not impossible, for many engineering problems. Couette and Poiseuille flow are two special cases in which these equations are greatly simplified into ordinary differential equations and exact solutions are possible. Both of these can be generalized as flow between infinite flat plates. Couette flow is where a fluid at rest between two flat plates is brought into motion by the movement of one of the plates as a result of a no-slip boundary condition. Poiseuille flow is where a fluid flows between two flat plates due to a pressure gradient and results in a parabolic velocity profile. The known solution of Poiseuille flow is used to validate the computer model developed in the previous chapter.

The parabolic velocity profile characteristic of a Poiseuille-type channel flow was used to validate the computer model presented in Chapter 3. Figure 4.1 shows the streamwise velocity profile from the numerical solution plotted against the analytically calculated parabolic profile. These two profiles are in excellent agreement, differing by 1.98% near the wall boundary and 0.23% at the center of the channel.

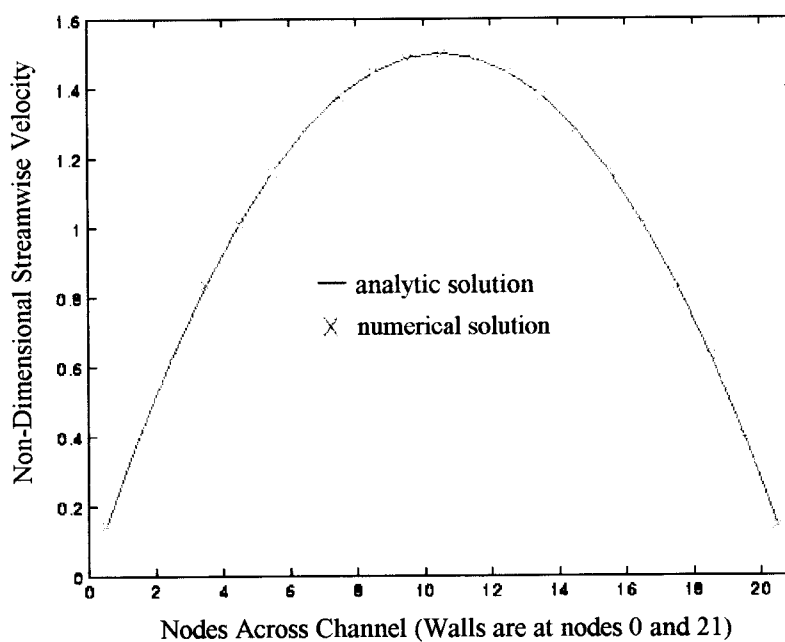


Figure 4.1 Comparison of analytic and numerical solution.

The entrance length of the developing flow was compared to theoretical predictions. From an order of magnitude analysis, the entrance length can be expressed in terms of the plate separation,  $D_p$ , and the Reynolds number (Bejan, 1995).

$$I \approx C \cdot D_p \cdot Re \quad (40)$$

Bejan gives the value of the constant  $C$  as 0.01 and reports values obtained by Sparrow and Schlichting of 0.026 and 0.04, respectively. Using evenly spaced nodes and noting that there are  $n_y$  momentum cells in the transverse direction, Eq. (40) can be expressed in terms of the number of momentum cells in the streamwise direction as:

$$i \approx C \cdot n_y \cdot Re \quad (41)$$

Figure 4.2 shows the developing velocity profiles for a  $Re=10$  flow with  $n_y=51$ . The velocity profile is fully developed after approximately 11 nodes. This corresponds to a value of 0.039 for the constant  $C$ , which is in agreement with the predicted values.

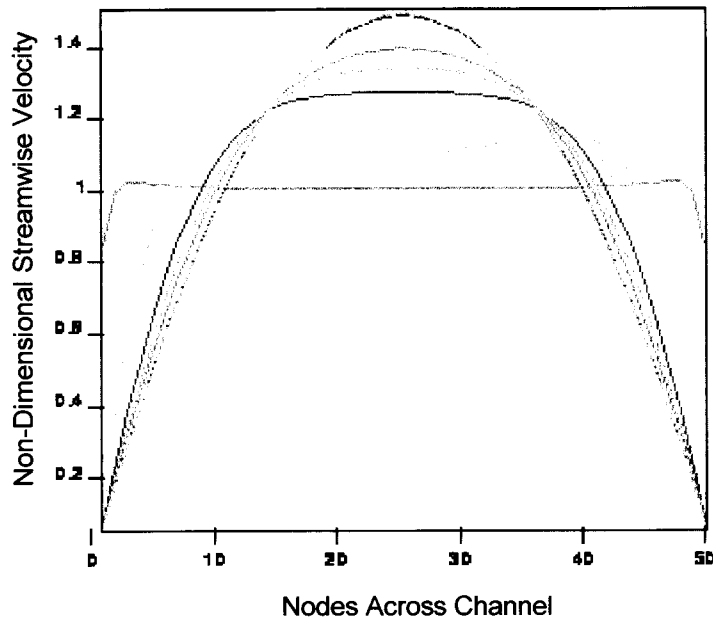


Figure 4.2 Developing velocity profiles for a flow with  $Re=10$  and  $Eu=1$ .

The input conditions used to model the Lorentz forces were to have two inlets, one for both fuel and oxidant with a wall separating them. The resulting pressure contours are shown below in Figure 4.3 and developing velocity profiles in Figure 4.4.

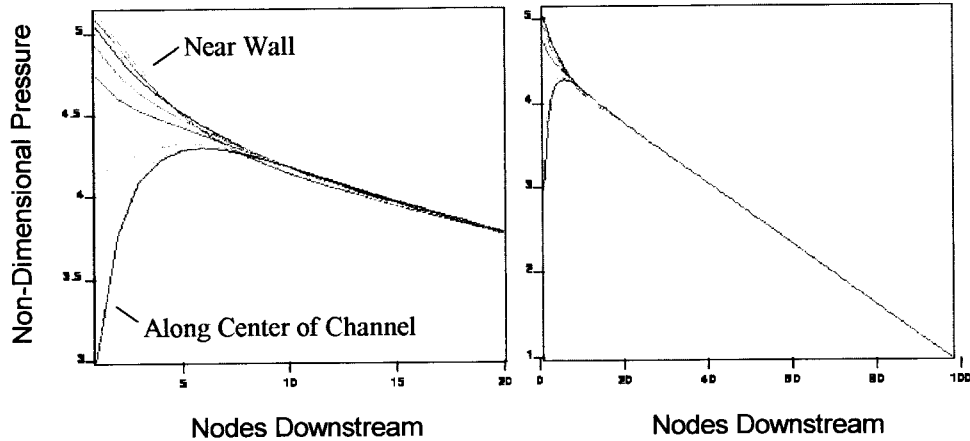


Figure 4.3 Non-dimensional pressure drop vs. downstream distance for dual inlet flow over (a) developing region and (b) full length of channel.

A check on the total mass flow rate and the divergence of the fluid velocity was done for transient and turbulent flow simulations since the analytical solution of Poiseuille flow is valid only for a steady-state, laminar flow. The numerical solutions showed a slight drop in the mass flow rate with distance down the channel. Almost the entire drop occurred at the inlet with a change of less than 0.01%.

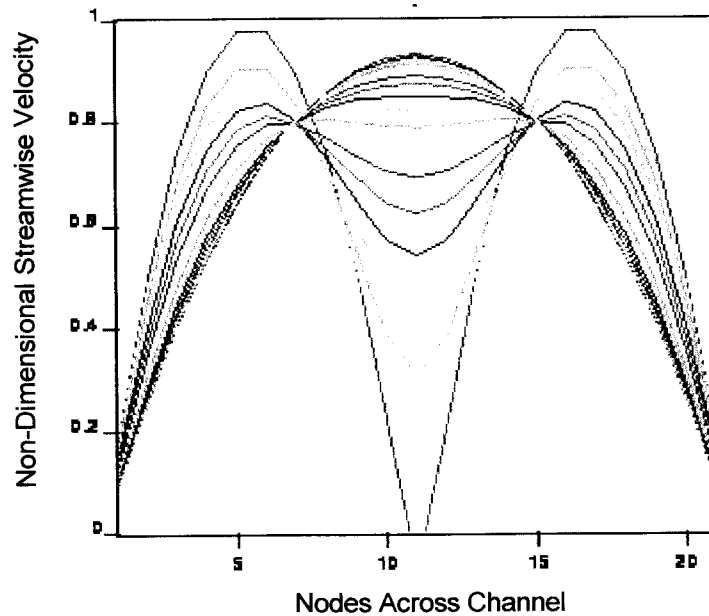


Figure 4.4 Developing velocity profiles for dual inlet flow.

### Design of Experiments

To characterize the results of numerical simulations, a statistical design and analysis of experiments (DOE) was used to evaluate the effectiveness of the mixing process with respect to the Euler number, Reynolds number, and the new non-dimensional parameter  $\Pi_1$ . Since the nature of the mixing process was undetermined, a three level design was selected to detect any quadratic or non-linear behavior. It is difficult to perform a standard  $3^k$  (k factors at 3 levels) factorial design because of the large number of runs that must be performed. In order to reduce the number of runs required, a Box-Behnken (Box et al., 1960) design was used. In addition to requiring a smaller number of runs, this design also lends itself well to fitting higher-order quantitative models to experimental data (Mohr et al., 1995).

The response variable selected to determine the effect of the three factors was the scalar mixedness parameter (Smith et al., 1995) defined by

$$M = \frac{A \cdot \int_A X(1-X)dA}{\left(\int_A X dA\right) \cdot \left(\int_A (1-X) dA\right)} \quad (42)$$

In this expression,  $X$  is the scalar mole fraction of a single species of a binary mixture and  $A$  is the area of interest. Eq. (42) may be interpreted by examining the integrand of the numerator under two conditions: (1) when only one species is present and (2) when equal amounts of both species are present. This function,  $X(1-X)$ , is equal to zero for the former case and the mixedness is undefined. This can be interpreted as no mixing. The maximum value of the function occurs when  $X$  is equal to one half and the mixedness is unity. Although  $M$  reduces to unity whenever  $X$  is constant over all of  $dA$ , this only has any physical meaning when there are equal amounts of species A and B present at all locations within  $dA$ . Thus, the mixedness parameter describes the relative amount of mixing between two species in a binary system and ranges in value between 0 and 1.

	$\Pi_1$	Re	Eu
+	0	10	0.5
o	5	15	1.0
-	10	20	1.5

Table 1. Levels of factors used in numerical simulations

The three non-dimensional parameters  $\Pi_1$ ,  $Re$ , and  $Eu$  were used to evaluate the mixedness parameter described above. The values used in the factorial design are summarized in Table 1, with 0 corresponding the nominal value and + / - corresponding to the values bracketing the nominal value. Completion of the design required a total of 15 simulation runs.

### Numerical Results

The numerical model of an incompressible gas flow subjected to Lorentz forces developed in the first part of this project was used to compute the scalar mixedness parameter defined above. Each simulation began with the same concentration of the seed species and was carried out the same distance in computational time. Contours of the species concentration are shown in Figure 4.5 for the different levels of Reynolds number and the maximum applied Lorentz force.

The results of the numerical computations are shown in the main effects and interactions plots of Figures 4.6 and 4.7, respectively. There are three points plotted for each factor. The three points represent the mean value of the mixedness parameter for all simulations performed with the value of the corresponding factor set at the high, low, and nominal value. The interactions plot has a format similar to the main effects plot, except that the interaction with a second factor is shown with lines which are labeled with the level of that factor. The scale of the vertical axis still represents the average level of mixedness parameter.

From the Figures 4.6 and 4.7, it appears that the mixedness is increased with increasing values of the non-dimensional parameter,  $\Pi_1$ , which represents the ratio of Lorentz forces to inertial forces. The mixedness also seems to increase with increasing Reynolds number. This is generally expected with higher Reynolds numbers. However, it is usually due to higher velocities. In the present case, increasing Reynolds numbers

would more often be associated with lower values of viscosity or high oscillation frequencies. It was surprising not to see some increase in mixedness with decreasing Euler numbers because a lower Euler number would seem to provide a less constrained flow and promote diffusion.

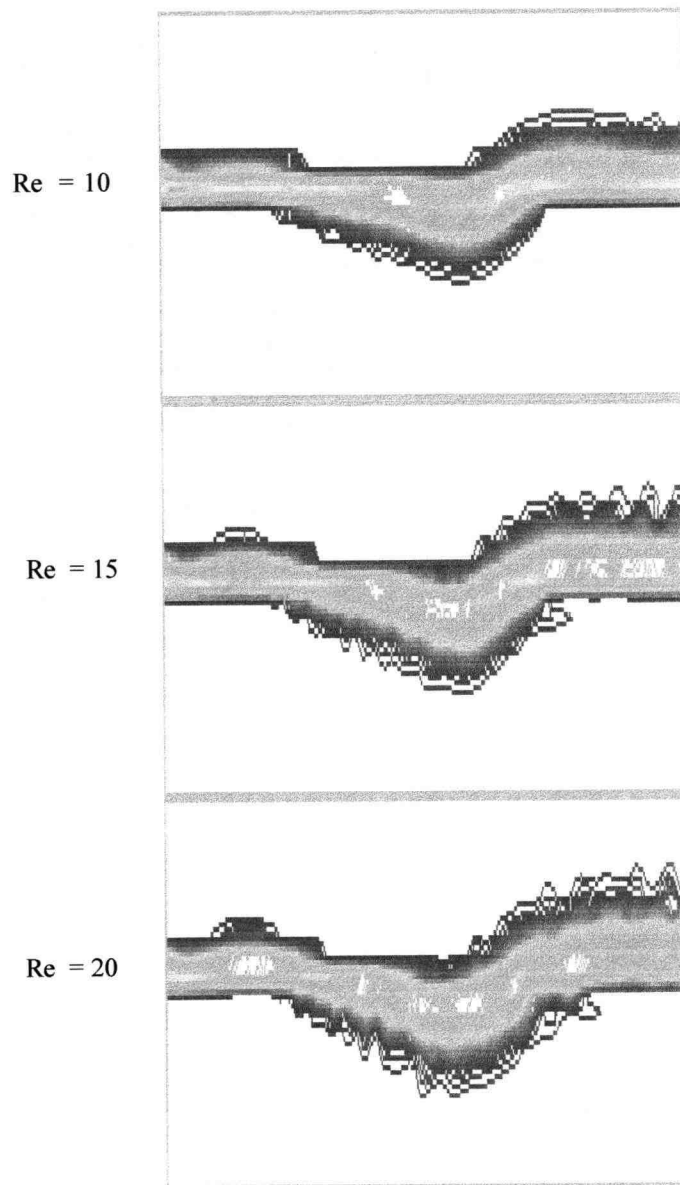


Figure 4.5 Species concentration for flows with  $Eu=1$  and  $\Pi_1 = 10$

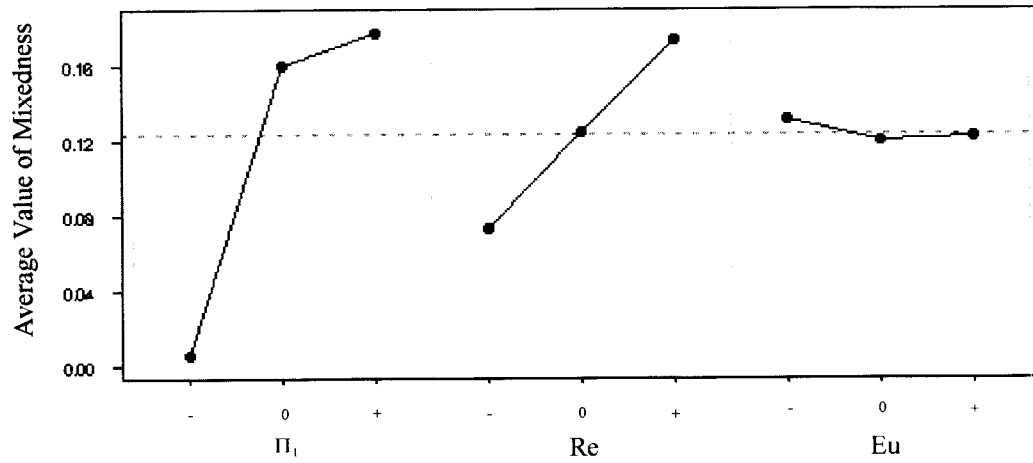


Figure 4.6 Main effects plot for non-dimensional flow parameters.

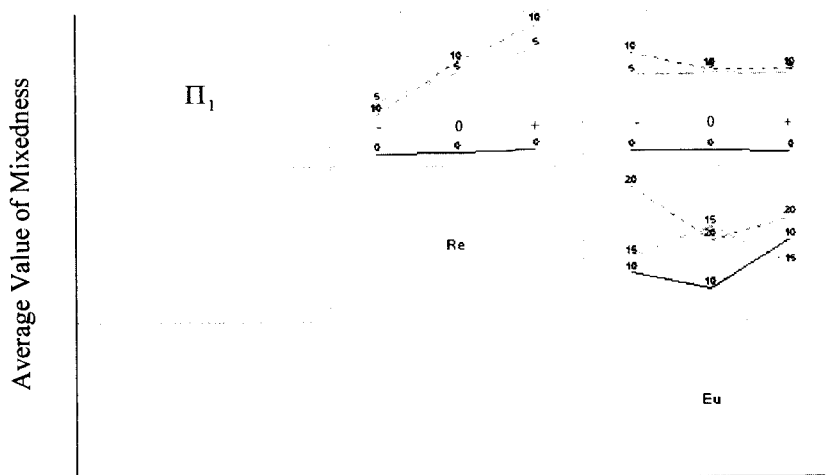


Figure 4.7 Interactions plot for non-dimensional flow parameters.

## APPLICATIONS

After performing numerical simulations, it was desired to design and build a burner which could be used to investigate the Lorentz mixing process. A design team was formed to construct a prototype burner and the design was then evaluated based on functional and material performance. A redesign was then done to improve both of these characteristics. The design of system components is outlined and two methods for seeding the reactant gasses were tested. It was found that using an aqueous solution produced conductivities three orders of magnitude higher than dry, non-solution methods. Finally, prospective experimental approaches for determining the effectiveness of the applied Lorentz forces are presented and their likeliness is evaluated based on known and expected constraints.

### Burner Design

The layout of the burner was based on a previous design (Wolfard and Parker, 1949) that used a slotted configuration to produce a laminar flame sheet. A burner used in previous Lorentz mixing experiments (Pattee and Peterson, 1993) was also based on this same design. It used a quartz material to insulate electrodes mounted on the burner, and was observed to wear heavily near the reaction zone. The primary concern in designing a burner to use in Lorentz mixing experiments is the environment in which the burner must operate. Not only are there concerns about durability, but the material selection is limited by the presence of electromagnetic fields. Since there were no benchmark data available to use as design targets, it was determined that a prototype burner would be constructed based on the main design requirements. Evaluation of the prototype burner was performed by repeated use over a range of operating conditions. After modifications were determined, a final burner was built and tested.

The primary design requirement was to produce a laminar flame sheet. The burner material also had to operate in a high temperature environment. Electrodes mounted on or near the burner had to be insulated from each other to prevent a short circuit through the burner material, which would preclude establishment of a current through the flame sheet. Other design requirements were to have the burner produce uniform flow of gases upon exiting the main flow channels, to eliminate extraneous reactions, to allow a clear view of the reaction zone, and to be able to adjust the position of the electrodes.

Two undergraduate mechanical engineering students performing a senior project formed a design team to build a prototype burner. The design team performed a materials search and employed a total quality management (TQM) approach based on the engineering requirements outlined above. Based on available material properties and the expected operating environment, zirconia ( $ZrO_2$ ) was selected. This ceramic material is available in rigid board form, has a very low electrical conductivity, a high operating temperature, and a porosity of 70%. With the exception of the high porosity, all of these properties were acceptable in terms of the design requirements outlined above.

Five 5.0 x 3.7 x 2.0 cm blocks (Figure 5.1) were precision machined by the manufacturer (Zircar, Inc.) to form four parallel flow channels. The inner two channels were for the reacting gases, while the exterior two gases were for a nitrogen shroud. The blocks were aligned to form the flow channels and were bonded together with a zirconia based cement for a matched coefficient of thermal expansion. This configuration allowed the first bonded seam to be placed 2 cm below the reaction zone to ensure the integrity of the joints. Since the material had a high porosity, a thin layer of cement was also coated on its surfaces to prevent diffusion of gas through the material.

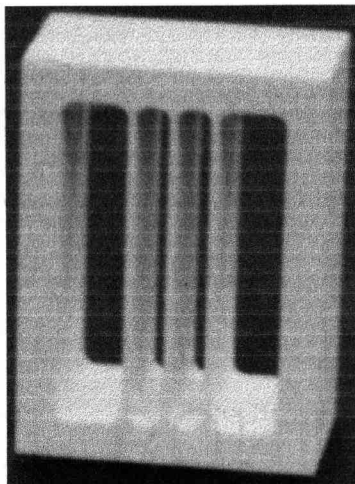


Figure 5.1 Machined ceramic block used to form flow channels.

The main flow channel assembly was mounted on a 10.0 x 7.0 x 2.5 cm aluminum base. Each flow channel received gas flow from three 3.5 mm diameter ports in the bottom of the base. Attached to the base were four aluminum plates which served as both a stand and housing for tubing connections. A drawing of the assembled burner is shown in Figure 5.2.

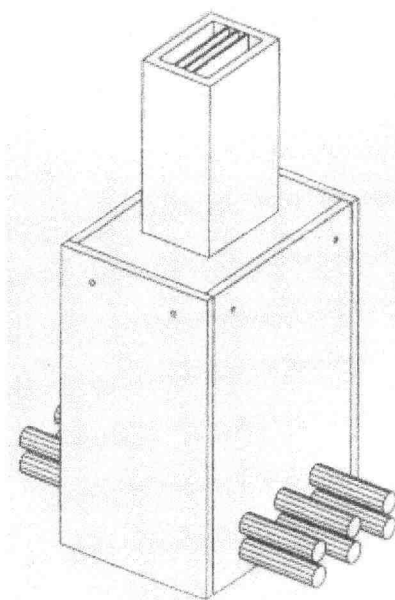


Figure 5.2 Drawing of assembled prototype burner.

Testing of the burner was done with flow rates ranging from 3 to 6 L/min. These corresponded to fluid velocities of 0.3 to 1.5 m/s, respectively. At lower values of the flow rate, the flow appeared to be laminar. However, at medium to high flow rates, the flame became turbulent and a clearly defined flame sheet was not visible. In addition, the coating of the burner with cementing material resulted in small irregularities of its surfaces. This caused the flame to attach preferentially to one side of the burner and inhibited the presence of a flame sheet. At higher flow rates the flame would detach from the burner completely, blow off would occur, and combustion would cease. After repeated use, minute cracks developed through the inner channel walls of the ceramic material. With the low flow velocities being considered, the possibility of premixing of the reactant streams prior to the exit plane increased. The flaws in the prototype burner were used as guideposts in preparing the final design.

## Redesigned Burner

The failure of the high temperature ceramic material required a complete re-design of the flow channel assembly. It was determined that machined stainless steel would be used. This would provide for both a durable material and a smooth, uniform surface for the flame to attach to. The design consisted of a main flow channel for the reacting gases with a surrounding channel to provide a shroud from the room air. To avoid the creation of large vortices, 20 gauge stainless sheet (~1.2 mm thick) was used to form the boundary between the fuel and oxidizer gases. Three 3.6 x 7.6 cm sheets were used for the main flow channels. These were held in place by two rectangular sides with 0.050 in (~1.3 mm) slots machined on their inner surfaces. The main flow channel assembly was formed by TIG welding the sheets to the sides (Figure 5.3).

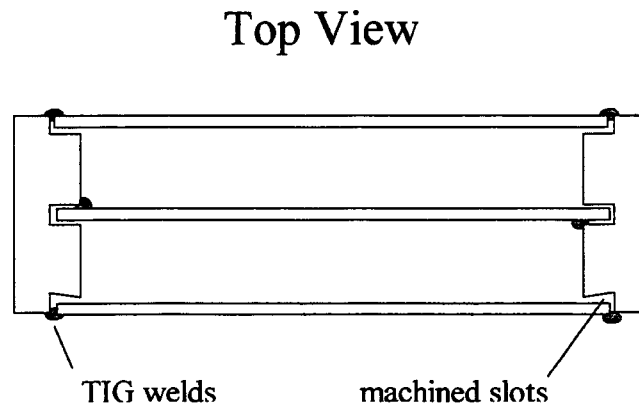


Figure 5.3 Flow channel assembly.

To aid in producing uniform flow, the gases entered the flow channels through 1.27 mm diameter guide veins which were drilled into the base of the burner (Figure 5.4). The base also had veins for the shroud gasses which flowed between the outside of the burner and an exterior duct. Gases entered through inlet ports, flowed through the guide veins and into the burner.

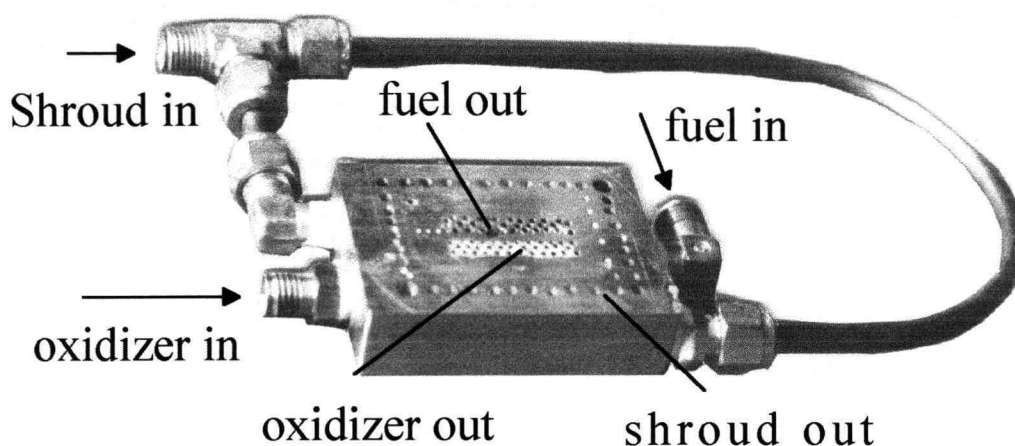


Figure 5.4 Base with guide veins and gas inlet ports.

The electrodes were mounted on the sides of the burner. To eliminate the problem of a short-circuit through the burner material, a 1 mm thick ceramic plate was cemented between the electrode mount and the burner with a high-temperature epoxy. The electrode mount is a two part design (Figure 5.5) which consists of a fixed U-shaped section mounted on the burner and an arm which is able to slide within and be locked with a set screw. The head of the slider arm has a sleeve that holds an electrode and the electrode is locked in place by tightening a set screw.

A surrounding shroud was formed from aluminum sheet. To minimize the total flow rate of shroud gas, the duct was tapered in from the base and extended up towards the burner exit with a constant area to aid in maintaining a laminar flow from the burner exit. The total cross-sectional area that the shroud gasses flowed through was  $2.72 \text{ cm}^2$  at the burner exit. The shroud and reactant gas flow rates were adjusted to match the velocities at the burner exit. The assembled burner is shown in Figure 5.6.

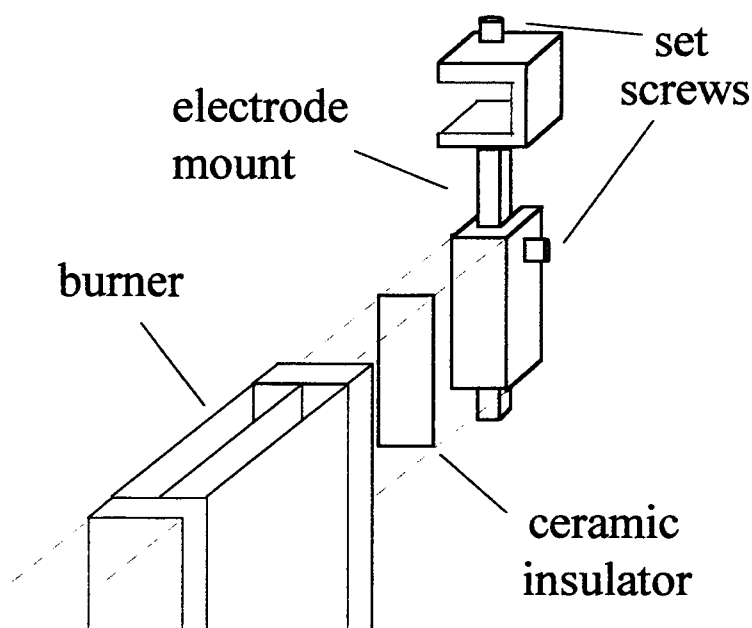


Figure 5.5 Two part adjustable electrode mount and assembly.

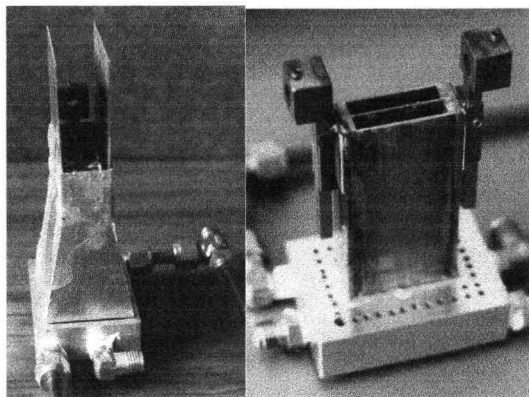


Figure 5.6 Burner with and without shroud.

The new burner performed well over a wide range of operating conditions. At extremely high flow rates, the flame sheet became turbulent, but over the flow rates being considered it was smooth and laminar.

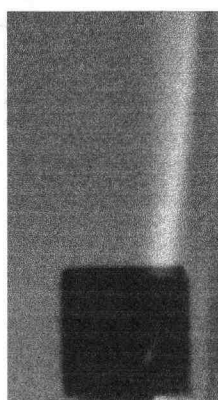


Figure 5.7 Laminar flame sheet.

The final burner did well in meeting the design requirements. The problem of flame detachment was not observed with the machined stainless steel design and there were no apparent signs of wear after testing. The only deficiency, in terms of design requirements, is that the electrode mounts do not give a clear view of the flame sheet near the electrodes (Figure 5.7). This could be easily remedied by machining the heads of the electrode mounts down and relocating the set screw which holds the electrode on the side.

### Seeding System

Group IA elements, Cs in particular, have been found to increase the electrical conductivity of gases by two to three orders of magnitude (Angrist, 1983). Seeding of materials into a flow stream can be done in many ways and is a common technique for flow visualization (Hancock and Lucht, 1995; Smith et. al., 1995). Group IA elements are most commonly found in crystalline form as salts. Although there are many ways of introducing the seed particles into the flow stream, there are only two forms in which a crystalline salt can be used: as a solid powder and as a liquid solution. The conductivity of seeded gases has a very strong temperature dependence. This made the former more attractive because it would avoid introducing water into the flame.

NaCl was used to test different designs for introducing the dry salt into the flow stream. The seed was first introduced into the flame in the form of a fine powder. The NaCl was held in a vertical tube. Air entered through the bottom of the tube, rose through the powder, and exited above carrying small amounts of salt with it. Attempts were made to correlate the amount of salt carried by the gas to the flow rate of the gas. This type of a fluidized bed configuration exhibits very nonlinear behavior and made calibration difficult. The mass of salt carried by the issuing gas was correlated to the gas flow rate, but a functional relationship could not be made due to variations from run to run. These variations could be attributed to residual buildup of seed material within the fuel/oxidizer piping system.

With this seeding system, currents carried by a hydrogen/air flame sheet were approximately  $8 \mu\text{A}$  and  $50 \mu\text{A}$  for NaCl and CsCl, respectively, which translated to an electrical resistance on the order of Megaohms. The current produced was five to six orders of magnitude less than that needed to create useful Lorentz forces. The current did not increase with increased amounts of seed material. It became apparent that the salt introduced into the flame was burning, rather than ionizing, and there was an insufficient number of charge carriers available to carry electrical current.

The seed was then introduced as an aqueous solution with the hope that the large numbers of ions would offset the reduced flame temperatures. This was done by atomizing the solution with an airbrush in a small mixing chamber (Figure 5.8). The air flow driving the brush's venturi created a mist and carried the salt into the flame. An air supply that bypassed the airbrush was added to increase the flow of air above the brushes limiting value of  $4.3 \text{ L/min}$ . The additional flow of air also delivered larger quantities of the mist into the flame.

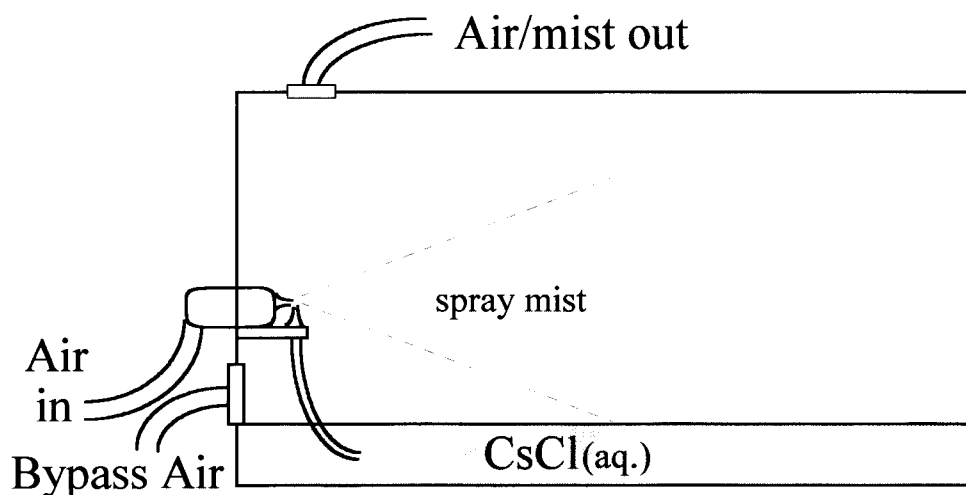


Figure 5.8 Schematic of seeding chamber.

The resulting currents were on the order of 10 mA, approximately three orders of magnitude higher than those created with the introduction of dry seed material. The desirable effect of increased currents was offset by limited operating times before the seed material would condense and clog the flow of air through the straightening veins in the base. While this was an improvement, the currents were still lower than required. Seeding the gases with an aqueous solution proved more effective than seeding in powder form. However, spraying the solution made it difficult to operate the burner for extended periods due to solid condensation of salt within the flow passages. Modification of the fuel delivery system to avoid small openings would likely eliminate this problem.

### Design Summary

The stainless steel flow channel and electrode mounts were practical designs which could be used in further experimental work with minor modification. The flow channel delivered the desired laminar flow for a wide range of gas flow rates, as compared to the prototype burner. The adjustable electrode mounts proved to be versatile enough to accommodate the use of different fuel types, since density variations of different fuels result in different location of the flame sheet. To enhance the visibility of the flame sheet, the heads of the electrode mounts could be machined down by approximately 40%.

The weakest design point of the newly constructed burner were the guide veins used to deliver the reactant gases to the flow channel. While producing a more uniform inlet velocity to the flow channel than the inlet ports of the prototype burner, the guide veins proved not to be a practical feature. For extended operating times and reduced maintenance, the previous design of Pattee and Peterson appears to be more promising. In this design the seeded gas entered the flow channel directly from a large mixing chamber.

## Proposed Experiments

Selection of quantitative variables which form a hypothesis from which the scientific method can be employed is the first step in planning an experimental endeavor. There are two variables which could be used to quantify the Lorentz mixing process. First, there is the scalar mixedness parameter described in Chapter 4. This variable can be used to evaluate the fluid dynamic aspects of the mixing process. Second is the flame temperature. This variable can be used to evaluate not only how well the reactant species are mixed, but also the additional energy released due to the application of the external forces. The two variables, mixedness and flame temperature, can be measured by two different experimental approaches.

The scalar mixedness parameter is a subjective variable. Its value is based upon the definition of an area or region of interest. This type of variable can be measured by a popular flow visualization technique, planar laser-induced fluorescence (PLIF) (Yang, 1989). PLIF has been used to determine combustion efficiencies by detecting the presence of OH radicals, as well as for visualizing fluid flow behavior (Arnold et al., 1990; Reichardt et al., 1995; Vandsburger et al., 1988).

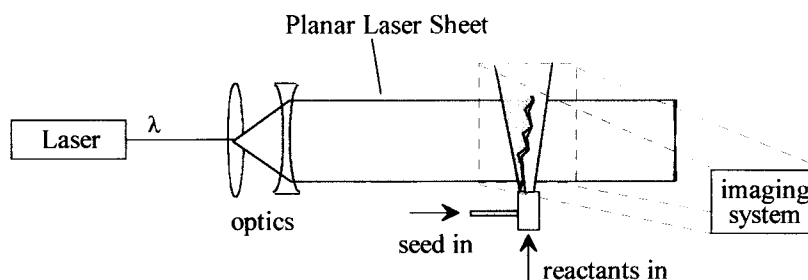


Figure 5.9 Schematic of PLIF experiment.

The basic principle behind both of these applications is that a laser is used to produce a wavelength of light which is known to cause a molecule present in the gas to fluoresce. The fluorescing molecule can be present either as a seed species or a combustion product. A schematic of the PLIF technique is demonstrated in Figure 5.9.

The PLIF technique would be an ideal method of visualizing flow behavior. The limitation of this technique for the application of Lorentz mixing is that combustion gases would be the required media due to the high temperature dependence of the gases electrical conductivity. For combustion flames, acetone has proved to be a good seed material (Smith et al., 1995; Lozano et al., 1994). The drawback of PLIF is the expensive equipment required. For example, a Nd:YAG laser with a frequency quadrupling crystal used to excite acetone costs tens of thousands of dollars. The optical imaging system required is an addition expense which makes this seemingly attractive technique somewhat less appealing.

Flame temperatures can be measured either by thermocouple probes (Pollock, 1984) or optical imaging systems (Pattee and Peterson, 1992; Bertagnotti et al., 1995). Thermocouple probes offer a cost effective method although there are difficulties in dealing with highly corrosive environments and accounting for radiation and conductive losses. Fortunately these problems are well known. Optical imaging systems using infrared (IR) spectra can also be used (Qian and Saito, 1995). This type of system can be purchased commercially for approximately ten thousand dollars.

Both optical temperature measurements using IR and PLIF imaging are subjective in nature. PLIF measurements can only be compared when they image the same physical area, while IR temperature measurements depend on the properties (emissivities) of the fluid and background source. Advances in modern imaging systems include devices that can detect or approximate needed emissivity values, which allows for fast and accurate temperature measurements.

## SUMMARY

Previous work on the use of Lorentz forces provided the basic motivation for developing a CFD tool that could be used to compute the effectiveness of the mixing process. The model was created by direct application of the governing equations of fluid flow. The estimation of the electric field and magnitude of the Lorentz force was a key part of this model. Unique non-dimensional parameters were introduced and an effort was made to compare their relative effects on fluid flows.

The CFD model was validated by comparing its results for simplified cases to exact analytical answers. A  $3^k$  Box-Behnken design of experiments was used to determine the factors which had a significant effect on the mixing process. The DOE was done using limited ranges of the factors in an effort to keep the size of the computational grid small and the time required for computation short. The non-dimensional Lorentz force parameter  $\Pi_1$  was shown to have the largest effect on the mixing process. The Reynolds number also displayed a positive effect, while the Euler number did not seem to affect the flow significantly. Further exploration of the effects of these factors should be done over wider ranges to gain a better understanding of their effect on flow behavior.

Finally, a burner that produced a laminar diffusion flame sheet was constructed and tested. Several important components of the burner were described, including a method for introducing a seed species into one of the reactant streams. Using CsCl as a seed material, currents on the order of 10 mA were observed to be carried by the flame sheet. This corresponded to a gas conductivity of approximately  $10^{-3}$  mho, which is about 3 orders of magnitude lower than what is required for appreciable Lorentz forces. An improved seeded gas delivery system could help to lower the resistance by reducing the amount of water entering the reaction zone and allowing extended operating times.

Two experimental approaches for evaluating the Lorentz mixing process were evaluated. PLIF measurements could be used to measure the scalar mixedness. This method requires a laser that produces a frequency which is known to excite a species present in the flow field. Data collection also requires a sophisticated imaging system. Flame temperature measurements can be done using thermocouple probes or IR imaging systems. Both flame temperature and mixedness measurements have difficulties which affect accuracy. It is not only important to consider the variable to be measured by a given experimental approach, but also how measurements are to be interpreted and how inaccuracies are to be accounted for. The ultimate choice of an experimental path should involve weighing the equipment costs and the known disadvantages against the expected results.

Future work in this area would be to modify the existing seeding and fuel delivery systems to increase the conductivity of the reacting gases. If that is done, an appropriate experimental approach could be implemented and experiments could be performed. Improvements to the existing computer code could be made to optimize its performance, thus requiring shorter lengths of time to perform simulations.

## BIBLIOGRAPHY

- Akay, H. U., 1990, *UCODE3 Users Manual Version 90.1*, Computational Fluid Dynamics Laboratory, Dept. of Mech. Eng., Purdue University - Indiana University at Indianapolis
- Anderson, J. D. Jr.; 1995, *Computational Fluid Dynamics: The Basics with Applications*, McGraw Hill, Inc., pp 248, 250-253
- Angrist, S. W., 1982, *Direct Energy Conversion*, Boston: Allyn and Bacon, Inc., pp 281-290
- Arnold, A., Becker, H., Hemberger, R., Hentschel, W., Ketterle, W., Kollner, M., Meienburg, W., Monkhouse, P., Neckel, H., Schafer, M., Schnider, K. P., Sick, V., Suntz, R., and Wolfrum, J., 1982, Laser in situ Monitoring of Combustion Processes, *Applied Optics*, Vol. 29, No. 33, pp 4860-4872
- Berman, H. A., Anderson, J. D. Jr., and Drummond, J. P., 1983, Supersonic Flow over a Rearward Facing Step with Transverse Nonreacting Hydrogen Injection, *AIAA Journal*, Vol. 27, No. 12, pp 1707-1713
- Box, G. E. P., and Behnken, D. W., 1960, Some New Three Level Designs for the Study of Quantitative Variables, *Technometrics*, Vol. 2, No. 2, pp 455-475
- Cramer, K. R. and Pal, Shih-I, 1973, *Magnetofluid Dynamics for Engineers and Applied Physicists*, Washington D.C.: Scripta Publishing Co., pp 4-6
- He, J. and Walker, J. D. A., 1995, A Note on the Baldwin-Lomax Turbulence Model, *ASME J. Fluids Eng.*, Vol. 117, pp 528-531
- Incropera, F. P., DeWITT, D. P., 1990, *Fundamentals of Heat and Mass Transfer*, New York: Wiley, pp 881-884
- Lozano, A., Smith, S. H., Mungaland, M. G., and Hanson, R. K., 1994, Concentration Measurements in a Transverse Jet by Planar Laser-Induced Fluorescence of Acetone, *AIAA Journal*, Vol. 32, No. 1, pp 218-221
- Mohr, J. W., Seyed-Yagoobi, J., and Page, R. H., 1995, Optimization of a Practical Radial Jet Reattachment Flame, *Proceedings of the 30th ASME Nat. Heat Trans. Conf.*, ASME-HTD, Vol. 2, pp 3-10
- Pattee, H. A. and Peterson, R. B., 1992, Flame Temperature Measurement by Monitoring an Alkali Emission Doublet Exposed to a Selectively Filtered Background Source, *ASME J. Heat Trans.*, Vol. 114, pp 630-635

- Pattee, H. A. and Peterson, R. B., 1993, Lorentz Mixing of Co-Flowing Reactant Streams, *Combust. Sci. Tech.*, Vol. 91, pp 297-307
- Pattee, H.A., Hager, M.B., and Thompson, J.I., 1996, Dimensional Analysis of Incompressible Fluid Flows Influenced by Oscillating Electromagnetic Forces, *Journal of Fluid Mechanics*, in review
- Pollock, D. D., 1984, Thermocouples in High-Temperature Reactive Atmospheres, *Combust. Sci. Tech.*, Vol. 42, pp 11-113
- Quian, C., and Saito, K., 1995, Measurements of Pool-Fire Temperature using IR Technique, *Proceedings of the Central and Western States (USA) Sections and Mexican National Section of the International Combustion Institute and American Flame Research Committee*, Paper 95S-017
- Reichart, T. A., Klassen, M. S., Kin, G. B., and Laurendeau, N. M., 1995, Measurements of Hydroxyl Concentrations and Lifetimes in Laminar Flames using Picosecond Time-Resolved Laser-Induced Fluorescence, *Proceedings of the Central and Western States (USA) Sections and Mexican National Section of the International Combustion Institute and American Flame Research Committee*, Paper 95S-028
- Smith, L. L., Delabroy, O., Lam, I. T., Majamaki, A. J., Karagozian, A. R., Marble, F. E., and Smith, O. I., 1995, PLIF Measurements of Mixing in a Loebed Injector, *Proceedings of the Central and Western States (USA) Sections and Mexican National Section of the International Combustion Institute and American Flame Research Committee*, Paper 95S-140
- Vandsburger, U., Seitzman, J. M., and Hanson, R. K., 1988, Visualization Methods for the Study of Unsteady Non-premixed Jet Flame Structure, *Cobust. Sci. Tech.*, Vol. 59, pp 455-461
- Welty, Wicks, and Wilson, 1984, *Fundamentals of Momentum, Energy, and Mass Transfer*, 3<sup>rd</sup> ed., New York: Wiley, pp 200-213
- Wolfard, H. G. and Parker, W. G., 1949, A New Technique for the Spectroscopic Examination of Flames at Normal Presures, *Proc. Phys. Soc.*, Vol. A62, pp 722
- Yang, W., 1989, *Handbook of Flow Visualization*, Hemisphere Publishing Corp., pp 219-231

## APPENDICES

**APPENDIX A**

## ELECTRODE PROBLEM: LAPLACE EQN.

-1 476 429 0 1 1 1 0 0

34

1 14 1 -0.012 0.001 -0.012 0.05 0.2

15 28 1 -0.0115 0.001 -0.0115 0.05 0.2

29 42 1 -0.011 0.001 -0.011 0.05 0.2

43 56 1 -0.0105774 0.0009063 -0.0105774 0.05 0.19

57 70 1 -0.0102929 0.0007071 -0.0102929 0.05 0.18

71 84 1 -0.0100937 0.0004226 -0.0100937 0.05 0.18

85 98 1 -0.01 0.0 -0.01 0.05 0.17

99 112 1 -0.0095 0.0 -0.0095 0.05 0.17

113 126 1 -0.0085 0.0 -0.0085 0.05 0.17

127 140 1 -0.0075 0.0 -0.0075 0.05 0.17

141 154 1 -0.0065 0.0 -0.0065 0.05 0.17

155 168 1 -0.0055 0.0 -0.0055 0.05 0.17

169 182 1 -0.0045 0.0 -0.0045 0.05 0.17

183 196 1 -0.0035 0.0 -0.0035 0.05 0.17

197 210 1 -0.0025 0.0 -0.0025 0.05 0.17

211 224 1 -0.0015 0.0 -0.0015 0.05 0.17

225 238 1 -0.0005 0.0 -0.0005 0.05 0.17

239 252 1 0.0005 0.0 0.0005 0.05 0.17

253 266 1 0.0015 0.0 0.0015 0.05 0.17

267 280 1 0.0025 0.0 0.0025 0.05 0.17

281 294 1 0.0035 0.0 0.0035 0.05 0.17

295 308 1 0.0045 0.0 0.0045 0.05 0.17

309 322 1 0.0055 0.0 0.0055 0.05 0.17

323 336 1 0.0065 0.0 0.0065 0.05 0.17

337 350 1 0.0075 0.0 0.0075 0.05 0.17

351 364 1 0.0085 0.0 0.0085 0.05 0.17

365 378 1 0.0095 0.0 0.0095 0.05 0.17

379 392 1 0.01 0.0 0.01 0.05 0.17

393 406 1 0.0100937 0.0004226 0.0100937 0.05 0.18

407 420 1 0.0102929 0.0007071 0.0102929 0.05 0.18

421 434 1 0.0105774 0.0009063 0.0105774 0.05 0.19

435 448 1 0.011 0.001 0.011 0.05 0.2

449 462 1 0.0115 0.001 0.0115 0.05 0.2

463 476 1 0.012 0.001 0.012 0.05 0.2

1

-1. -1. 0. 0. 0. 0. 0.

13

1 417 13 14 4 2 1 15 16 2 1

2 418 13 14 4 2 1 16 17 3 2

3 419 13 14 4 2 1 17 18 4 3

4 420 13 14 4 2 1 18 19 5 4

5 421 13 14 4 2 1 19 20 6 5

6 422 13 14 4 2 1 20 21 7 6

7 423 13 14 4 2 1 21 22 8 7

8 424 13 14 4 2 1 22 23 9 8

9 425 13 14 4 2 1 23 24 10 9

10 426 13 14 4 2 1 24 25 11 10

11 427 13 14 4 2 1 25 26 12 11

12 428 13 14 4 2 1 26 27 13 12

13 429 13 14 4 2 1 27 28 14 13

0

2

1 85 14 100

379 463 14 -100

0

END

**APPENDIX B**

```

program profile
implicit none
integer nnx, nny
parameter(nnx=100, nny=42)
integer ny, i, j, D
real*8 dx, dy, u, x, y, uIN, vIN, Pin
dimension u(1:nnx, 0:nny), uIN(0:nny), vIN(1:nny),
#      Pin(0:nny), x(0:nnx), y(0:nny)

D=ny/4
print*, "D=", D
ny=ny-1
dy=1.0/float(ny)
dx=dy
do 4 j=0, D
  uIN(D+22 + j)=1.0*( 1.0 - ( ( float(j)+0.5)/float(D) )**2.0)
  uIN(D+1 + j)=1.0*( 1.0 - ( ( float(j)+0.5)/float(D) )**2.0)
4 continue
do 5 j=0, D
  uIN(D+21 - j)=1.0*( 1.0 - ( ( float(j)+0.5)/float(D) )**2.0)
  uIN(D - j)=1.0*( 1.0 - ( ( float(j)+0.5)/float(D) )**2.0)
5 continue
uIN(0)=(-1.0)*uIN(1)
uIN(nny/2)=(-0.5)*(uIN((nny/2)+1)+uIN((nny/2)-1))
uIN(nny)=(-1.0)*uIN(ny)

do 20 i=0, nnx
  x(i)=(float(i)-float(nnx/4))*(dx)
  do 10 j=0, nny
    y(j)=(float(j)-(float(nny)/2.0))*(dy)
    if (i.GT.0) u(i, j)=uIN(j)
    if (j.GT.0) vIN(j)=0.0
    Pin(j)=1.0
10 continue
20 continue

open(unit=22, file="XX2.dat")
open(unit=33, file="UX2.dat")
rewind(22)
rewind(33)
C ***** WRITING X, Y, Z FILE 'iX.dat' FOR PLOT3D FORMAT *****
WRITE(22, *) nnx, nny+1, 1
WRITE(22, *) ((X(I), I=1, nnx), J=0, nny)
WRITE(22, *) ((Y(J), I=1, nnx), J=0, nny)
WRITE(22, *) ((1.0, I=1, nnx), J=0, nny)
REWIND(22)
CLOSE(22)
C ***** WRITING Q FILE 'iQ.dat' FOR PLOT3D FORMAT *****
WRITE(33, *) nnx, nny+1, 1
WRITE(33, *) 0.00125, 1.57, 1, 1
WRITE(33, *) ((u(i, j), I=1, nnx), J=0, nny)
WRITE(33, *) ((1.0, I=1, nnx), J=0, nny)
REWIND(33)
CLOSE(33)
open(unit=44, file='profile.dat')
rewind(44)
write(44, *) (Pin(j), j=0, nny)

```

```
write(44,*)(uIN(j),j=0,nny)
write(44,*)(vIN(j),j=1,nny)
rewind(44)
close(44)
do 30 j=0,nny
print*,uIN(j)
30 continue
end
```

APPENDIX C

```

*****
C Program:   CFD1.f
C Author:    Michael Hager
C Date:      December 10, 1996
C Description: This program solves for the velocity and pressure fields
C             of 2-D incompressible flow subjected to a time varying
C             Lorentz force in the entrance region between infinite,
C             flat, parallel plates using the SIMPLER algorithm
*****

```

```

program CFD1
implicit none
integer nnx, nny
parameter(nnx=100, nny=42)
integer k, l, m, nx, ny, NT, nCYCLES, nHOOPS, iv, jv, numout
real*8 u, v, P, uProv, vProv, Pprov, uOLD, vOLD, B, Div, status, x, y,
# dx, dy, dt, Re, t, acc, goodDiv, maxDiv, maxU, maxV, Fmag, worstv,
# uIN, vIN, Pin, c, Dcs, mu, mut, Dft, LF, Mix, Eu, rho, rads, Zo, FXON
dimension u(1:nnx, 0:nny), uProv(1:nnx, 0:nny),
# v(0:nnx-1, 1:nny), vProv(0:nnx-1, 1:nny),
# uOLD(1:nnx, 0:nny), vOLD(0:nnx-1, 1:nny),
# P(0:nnx-1, 0:nny), Pprov(0:nnx-1, 0:nny),
# B(0:nnx-1, 0:nny), Div(0:nnx-1, 0:nny),
# Fmag(0:nnx, 0:nny), uIN(0:nny), vIN(1:nny),
# Pin(0:nny), c(0:nnx-1, 0:nny), Dft(1:nnx-1, 1:nny-1),
# Re(1:nnx-1, 1:nny-1), x(0:nnx), y(0:nny)

open(unit=3, file="cnvrg.dat")
rewind(3)
open(unit=9, file="mix.dat")
rewind(9)

C INITIALIZE VARIABLES
nx=nnx-2
ny=nny-1
print*, "Enter NT: "
read*, NT
nCYCLES=32
nHOOPS=100
print*, "Enter the magnitude of the force: "
read*, LF
acc=1.0D-3
goodDiv=1.0D-1
maxU=0.0
maxV=0.0
t=0.0
call initit(nnx, nny, ny, nCYCLES, nHOOPS, x, y, dx, dy, dt, rads, Zo,
# u, v, P, uProv, vProv, Pprov, uOLD, vOLD, B, Div, rho,
# Fmag, uIN, vIN, Pin, c, Dcs, Re, mu, mut, Dft, LF, Eu)
call boundary(nnx, nny, nx, ny, u, v, P, uIN, vIN, Pin)
do 300 k=1, NT
open(unit=2, file="field.dat")
open(unit=4, file="div.dat")
rewind(2)
rewind(4)
worstv=0.0
numout=0
status = (float(k)/float(NT))*100.0
FXON=0.0
if (k.GT.1) FXON=1.0

```



```

#      P(0:nnx-1,0:nny),Pprov(0:nnx-1,0:nny),Pin(0:nny),
#      B(0:nnx-1,0:nny),Div(0:nnx-1,0:nny).
#      Fmag(0:nnx,0:nny),x(0:nnx),y(0:nny).
#      c(0:nnx-1,0:nny),Dft(1:nnx-1,1:nny-1),
#      Re(1:nnx-1,1:nny-1),mut(1:nnx-1,1:nny-1)

maxf=0.0
f=60.0
w=2.0*PI*f
dy=1.0/(float(ny))
dx=dy
dt=2.0*PI/(float(nCYCLES)*float(nHOOPS))
print*,"Enter the Reynold's #: "
read* ,ReI
print*,"Enter the Euler #: "
read* ,Eu
Zo=0.011
z=1.0
Dcs=(3.684D-4)/(w*0.00948847)
rho=0.1707
mu=(rho*Zo*(w*Zo)**2.0)/ReI
open(unit=24,file='profile.dat')
rewind(24)
read(24,*)(Pin(j),j=0,nny)
read(24,*)(uIN(j),j=0,nny)
read(24,*)(vIN(j),j=1,nny)
rewind(24)
close(24)

do 20 i=0,nnx
  x(i)=(float(i)-float(nnx/4))*(dx)
  do 10 j=0,nny
    y(j)=(float(j)-(float(nny)/2.0))*(dy)
    if (i.GT.0) then
      u(i,j)=uIN(j)
      uProv(i,j)=u(i,j)
      uOLD(i,j)=0.0
      if (i.LT.nnx) then
C MAKE SURE THIS LINE MATCHES THE SAME LINE IN difsnbc SUBROUTINE
        if ( (j.GT.19).AND.(j.LT.23) ) then
          c(i,j)=1.0
        else
          c(i,j)=0.0
        endif
      endif
    endif
    if ( (i.LT.nnx).AND.(j.GT.0) ) then
      v(i,j)=vIN(j)
      vProv(i,j)=v(i,j)
      vOLD(i,j)=0.0
      if ( (i.GT.0).AND.(j.LT.nny) ) then
        Dft(i,j)=0.0
        mut(i,j)=0.0
        Re(i,j)=ReI
      endif
    endif
  endif
  if (i.LT.nnx) then
    P(i,j)=Pin(j)
    Pprov(i,j)=P(i,j)
    B(i,j)=0.0
  endif

```

```

        Div(i,j)=0.0
    endif
    Fmag(i,j)=LF/((x(i)**2.0+y(j)**2.0+z**2.0)**1.5)
    if (Fmag(i,j).GT.maxf) maxf=Fmag(i,j)
10  continue
20  continue

    return
end

```

\*\*\*\*\*

```

subroutine boundary(nnx,nny,nx,ny,u,v,P,uIN,vIN,Pin)
implicit none
integer nnx,nny,nx,ny,i,j
real*8 u,v,P,uIN,vIN,Pin
dimension u(1:nnx,0:nny),v(0:nnx-1,1:nny),P(0:nnx-1,0:nny),
#      uIN(0:nny),vIN(1:nny),Pin(0:nny)

C  FIXED INLET AND MIRRORED EXIT BOUNDARY CONDITIONS FOR VELOCITIES
C  MIRRORED INLET AND EXTRAPOLATED EXIT BOUNDARY CONDITIONS FOR PRESSURE
do 10 j=0,ny+1
    u(1,j)=uIN(j)
    u(nx+2,j)=u(nx,j)
    P(0,j) = Pin(j)
    P(nx+1,j)= 2.0*P(nx,j)-P(nx-1,j)
10  continue
do 15 j=1,ny+1
    v(0,j)=vIN(j)
    v(nx+1,j)=v(nx,j)
15  continue
C  NO-SLIP WALL BOUNDARY CONDITIONS FOR VELOCITIES
C  MIRRORED WALL BOUNDARY CONDITIONS FOR PRESSURE
do 20 i=0,nx+2
    if (i.GT.0) then
        u(i,0)=-u(i,1)
        u(i,ny+1)=-u(i,ny)
    endif
20  continue
do 25 i=0,nx+1
    v(i,1)=0.0
    v(i,ny+1)=0.0
    P(i,0) = P(i,1)
    P(i,ny+1) = P(i,ny)
25  continue

    return
end

```

\*\*\*\*\*

```

subroutine diffusion(nnx,nny,nx,ny,u,v,c,dx,dy,dt,Dcs,Dft,HOOP)
implicit none
integer nnx,nny,nx,ny,i,j,tstep,nstep,HOOP,x,y
real*8 u,v,c,dx,dy,dt,Dft,Dcs,cOLD,cNEW,m,A,ddt,cOUT,
#      uAVG,vAVG
dimension u(1:nnx,0:nny),v(0:nnx-1,1:nny),c(0:nnx-1,0:nny),
#      Dft(1:nnx-1,1:nny-1),x(1:nnx-1),y(1:nny-1),
#      cOUT(0:nnx-1,0:nny)

```

```

A=(dx/dy)**2.0
nstep=100
ddt=dt/nstep
do 30 tstep=1,nstep
  call difsnbc(nnx,nnx,ny,ny,c)
do 20 i=1,nnx
  do 10 j=1,ny
    uAVG = (u(i,j)+u(i+1,j))/2.0
    vAVG = (u(i,j)+u(i,j+1))/2.0
    cOLD=c(i,j)
    m=((Dcs+Dft(i,j))/(dx*dx))
    * ((c(i+1,j)-2.0*c(i,j)+c(i-1,j))
    * + A*(c(i,j+1)-2.0*c(i,j)+c(i,j-1)))
    * - (uAVE*(c(i+1,j)-c(i-1,j))/dx
    * +vAVE*(c(i,j+1)-c(i,j-1))/dy )
    cNEW=cOLD + m*ddt
    if (cNEW.LT.0.0) cNEW=0.0
    if (cNEW.GT.1.0) cNEW=1.0
    cOUT(i,j)=cNEW
    if (cOUT(i,j).LT.1.0D-6) cOUT(i,j)=0.0
    c(i,j)=cNEW
  10 continue
20 continue
30 continue
  do 35 j=1,nnx-1
    y(j)=j
  35 continue
  do 36 i=1,nnx-1
    x(i)=i
  36 continue
  if (HOOP.EQ.50) then
    open(unit=22,file="fxX.dat")
    open(unit=33,file="fx.dat")
    rewind(22)
    rewind(33)
  C ***** WRITING X,Y,Z FILE 'iX.dat' FOR PLOT3D FORMAT *****
    WRITE(22,*)nnx-1,nnx-1,1
    WRITE(22,*)((x(i),I=1,nnx-1),J=1,nnx-1))
    WRITE(22,*)((y(j),I=1,nnx-1),J=1,nnx-1))
    WRITE(22,*)((1.0,I=1,nnx-1),J=1,nnx-1))
    REWIND(22)
    CLOSE(22)
  C ***** WRITING Q FILE 'iQ.dat' FOR PLOT3D FORMAT *****
    WRITE(33,*)nnx-1,nnx-1,1
    WRITE(33,*)0.00125,1.57,1,1
    WRITE(33,*)((cOUT(i,j),I=1,nnx-1),J=1,nnx-1))
    WRITE(33,*)((u(i,j),I=1,nnx-1),J=1,nnx-1))
    WRITE(33,*)((v(i,j),I=1,nnx-1),J=1,nnx-1))
    WRITE(33,*)((Dft(i,j),I=1,nnx-1),J=1,nnx-1))
    WRITE(33,*)((1.0,I=1,nnx-1),J=1,nnx-1))
    REWIND(33)
    CLOSE(33)
  endif

  return
end

*****

subroutine difsnbc(nnx,nnx,ny,ny,c)

```

```

implicit none
integer nnx, nny, nx, ny, i, j
real*8 c
dimension c(0:nnx-1, 0:nny)

C INLET BOUNDARY CONDITION
do 10 j=1, nny
  if (j.GT.19).AND.(j.LT.23) then
    c(0,j)=1.0
  else
    c(0,j)=0.0
  endif
10 continue
C EXIT BOUNDARY CONDITION
do 20 j=1, nny
  c(nnx-1,j)=2.0*c(nx,j)-c(nx-1,j)
20 continue
c SIDE (WALL) BOUNDARY CONDITIONS
do 30 i=1, nnx-1
  c(i,0)=c(i,1)
  c(i,nny)=c(i,ny)
30 continue

return
end

*****

subroutine predict(nnx, nny, nx, ny, dx, dy, dt, t, Re, Eu,
# u, v, P, uProv, vProv, Pprov, Fmag, c, FXON)
implicit none
integer nnx, nny, nx, ny, i, j
real*8 dx, dy, dt, Re, Eu, t, Fmag, c, FXON,
# u, v, P, uProv, vProv, Pprov,
# dPdx, dPdy,
# d2udx2, d2udy2, d2vdx2, d2vdy2, Sx, Sy,
# uLeftX, uRightX, vTopX, vBottomX,
# uuLeft, uuRight, uvTop, uvBottom,
# uLeftY, uRightY, vTopY, vBottomY,
# vvTop, vvBottom, uvLeft, uvRight,
# duudx, duvdy, duvdx, dvvdy
dimension u(1:nnx, 0:nny), uProv(1:nnx, 0:nny),
# v(0:nnx-1, 1:nny), vProv(0:nnx-1, 1:nny),
# P(0:nnx-1, 0:nny), Pprov(0:nnx-1, 0:nny),
# Fmag(0:nnx, 0:nny), c(0:nnx-1, 0:nny),
# Re(1:nnx-1, 1:nny-1)
C SOLVE FOR X VELOCITY COMPONENT
do 20 i=2, nx+1
  do 10 j=1, nny
C ASSIGN OLD TIME STEP VALUE OF PRESSURE TO PROVISIONAL VALUE
Pprov(i,j) = P(i,j)
C CALCULATE FLUX TERMS AND DERIVATIVES FOR X-MOMENTUM EQUATION
uLeftX = ( u(i,j)+u(i-1,j) )/2.0
uRightX = ( u(i+1,j)+u(i,j) )/2.0
vTopX = ( v(i-1,j+1)+v(i,j+1) )/2.0
vBottomX = ( v(i-1,j)+v(i,j) )/2.0
uuLeft = ((uLeftX + dabs(uLeftX))/2.0)*u(i-1,j)
# +((uLeftX - dabs(uLeftX))/2.0)*u(i,j)
uuRight = ((uRightX + dabs(uRightX))/2.0)*u(i,j)
# +((uRightX - dabs(uRightX))/2.0)*u(i+1,j)

```

```

      uvTop = ( vTopX + dabs(vTopX) )/2.0 *u(i,j)
#      +( vTopX - dabs(vTopX) )/2.0 *u(i,j+1)
      uvBottom = ( vBottomX + dabs(vBottomX) )/2.0 *u(i,j-1)
#      +( vBottomX - dabs(vBottomX) )/2.0 *u(i,j)
      duudx = ( uuRight-uuLeft )/dx
      duvdy = ( uvTop-uvBottom )/dy
      dPdx = ( P(i,j)-P(i-1,j) )/dx
      d2udx2 = ( u(i+1,j)-2.0*u(i,j)+u(i-1,j) )/(dx*dx)
      d2udy2 = ( u(i,j+1)-2.0*u(i,j)+u(i,j-1) )/(dy*dy)
      Sx=(1.0/Re(i,j))*(d2udx2+d2udy2) - duudx - duvdy
      uProv(i,j) = u(i,j) + dt*( Sx - Eu*dPdx )
10  continue
20  continue

C  SOLVE FOR Y VELOCITY COMPONENT
do 40 i=1,nx
do 30 j=2,ny
C  ASSIGN OLD TIME STEP VALUE OF PRESSURE TO PROVISIONAL VALUE
Pprov(i,j) = P(i,j)
C  CALCULATE FLUX TERMS AND DERIVATIVES FOR Y-MOMENTUM EQUATION
uLeftY = ( u(i,j)+u(i,j-1) )/2.0
uRightY = ( u(i+1,j)+u(i+1,j-1) )/2.0
vTopY = ( v(i,j)+v(i,j+1) )/2.0
vBottomY = ( v(i,j)+v(i,j-1) )/2.0
vvTop = ((vTopY + dabs(vTopY))/2.0)* v(i,j)
#      +((vTopY - dabs(vTopY))/2.0)* v(i,j+1)
vvBottom = ((vBottomY + dabs(vBottomY))/2.0)*v(i,j-1)
#      +((vBottomY - dabs(vBottomY))/2.0)*v(i,j)
uvLeft = ((uLeftY + dabs(uLeftY))/2.0)*v(i-1,j)
#      +((uLeftY - dabs(uLeftY))/2.0)*v(i,j)
uvRight = ((uRightY + dabs(uRightY))/2.0)*v(i,j)
#      +((uRightY - dabs(uRightY))/2.0)*v(i+1,j)
duvdx = ( uvRight-uvLeft )/dx
dvvdy = ( vvTop-vvBottom )/dy

      dPdy = ( P(i,j)-P(i,j-1) )/dy

      d2vdx2 = ( v(i+1,j)-2.0*v(i,j)+v(i-1,j) )/(dx*dx)
      d2vdy2 = ( v(i,j+1)-2.0*v(i,j)+v(i,j-1) )/(dy*dy)

      Sy=( 1.0/Re(i,j))*(d2vdx2+d2vdy2)-duvdx-dvvdy )
      vProv(i,j) = v(i,j) +
#      dt*( Sy - Eu*dPdy +
#      FXON*c(i,j)*Fmag(i,j)*Dsin(t)
30  continue
40  continue

do 60 i=1,nx
do 50 j=1,ny
Pprov(i,j)=P(i,j)
50  continue
60  continue

return
end

*****

subroutine correct(nnx,nny,nx,ny,u,v,P,uProv,vProv,
#      Pprov,B,dx,dy,dt,maxU,maxV)

```

```

implicit none
integer nnx, nny, nx, ny, i, j
real *8 u, uProv, v, vProv, P, Pprov, B, dBdx, dBdy, dx, dy, dt, maxU, maxV
dimension u(1:nnx, 0:nny), uProv(1:nnx, 0:nny),
#      v(0:nnx-1, 1:nny), vProv(0:nnx-1, 1:nny),
#      P(0:nnx-1, 0:nny), Pprov(0:nnx-1, 0:nny),
#      B(0:nnx-1, 0:nny)

maxU=0.0
maxV=0.0

C SOLVE FOR PRESSURE OVER i=1,nx AND j=1,ny
do 20 i=1,nx
do 10 j=1,ny
P(i,j) = Pprov(i,j) + B(i,j)/dt
Pprov(i,j)=P(i,j)
10 continue
20 continue

C SOLVE FOR v OVER i=1,nx AND j=2,ny
do 40 i=1,nx
do 30 j=2,ny
dBdy = ( B(i,j)-B(i,j-1) )/dy
v(i,j) = vProv(i,j) - dBdy
vProv(i,j)=v(i,j)
if ( v(i,j).GT.maxV ) maxV=v(i,j)
30 continue
40 continue

C SOLVE FOR u OVER i=2,nx+1 AND j=1,ny
do 60 i=2,nx+1
do 50 j=1,ny
dBdx = ( B(i,j)-B(i-1,j) )/dx
u(i,j) = uProv(i,j) - dBdx
uProv(i,j)=u(i,j)
if ( u(i,j).GT.maxU ) maxU=u(i,j)
50 continue
60 continue

return
end

```

\*\*\*\*\*

```

subroutine divergence(nnx, nny, nx, ny, Div, u, v, dx, dy, maxDiv)
implicit none
integer nnx, nny, nx, ny, i, j
real*8 Div, u, v, dx, dy, maxDiv, dudx, dvdy
dimension Div(0:nnx-1, 0:nny), u(1:nnx, 0:nny), v(0:nnx-1, 1:nny)

maxDiv=0.0
C CALCULATE DIVERGENCE OVER NODES 1,nx AND 1,ny
do 20 i=1,nx
do 10 j=1,ny
dudx = ( u(i+1,j)-u(i,j) )/dx
dvdy = ( v(i,j+1)-v(i,j) )/dy
Div(i,j) = dudx + dvdy
if( dabs( Div(i,j) ).GT.maxDiv ) maxDiv=dabs( Div(i,j) )
10 continue
20 continue

```

```

return
end

```

```

*****

```

```

subroutine SOR(nnx, nny, nx, ny, f, acc, dx, dy, C)
implicit none
integer nnx, nny, nx, ny, i, j, n1, n2, dn, m1, m2, dm, iter, count
real *8 f, acc, dx, dy, C,
#   absError, error, A, fOld, fNew, w, direction
dimension f(0:nnx-1, 0:nny), C(0:nnx-1, 0:nny)

acc=acc
A=(dx/dy)**2.0
w=0.8
absError=1.0
error=0.0
iter = 0
direction = 1.0
C RESET SOLUTIONN VARIABLE TO ZERO TO BEGIN SOLUTION
do 2 i=0, nx-1
do 1 j=0, ny-1
f(i, j)=0.0
1 continue
2 continue
count=0
C ITERATE ON SOLUTION UNTIL VALUES DONT CHANGE
do 30 while ( ( absError.GT.acc ) )
count=count+1
absError=0.0
C CHANGE DIRECTION EACH ITERATION FROM
C FORWARD.BACKWARD TO BACKWARD.FORWARD
if (direction.EQ.1) then
n1=1
n2=nx
dn=1
m1=ny
m2=1
dm=-1
else
n1=nx
n2=1
dn=-1
m1=1
m2=ny
dm=1
endif
C CALCULATE VALUES OF BETA OVER NODES 1.nx AND 1.ny
do 20 i=n1, n2, dn
do 10 j=m1, m2, dm
iter = iter + 1
fOld = f(i, j)
fNew = ( ( f(i+1, j)+f(i-1, j) ) +
#   A*( f(i, j+1)+f(i, j-1) ) - dx*dx*C(i, j) ) /
#   ( 2.0*(1.0 + A ) )
fNew = w*fNew + (1.0-w)*fOld
error=dabs( ( fNew-fOld)/fNew )
if ( error.GT.absError ) absError = error
f(i, j) = fNew

```

```

C   APPLY FIXED INLET AND ZERO DERIVATIVE EXIT B.C.'s
C   Pin is fixed => Bin=0; dudx=0 at exit => d2Bdx2=0
   if ( i.EQ.1 ) f(i-1,j) = 0.0
   if ( i.EQ.nx ) f(i+1,j) = 2.0*f(i,j) - f(i-1,j)
10  continue
C   APPLY MIRRORED BOUNDARY CONDITIONS AT WALLS
   f(i,0) = f(i,1)
   f(i,ny+1) = f(i,ny)
20  continue
   direction=(-1.0)**(1.0*iter)
   if (count.GT.25000) then
     absError=0.0
     print*,'maxed out'
   endif
30  continue

   return
   end

```

\*\*\*\*\*

```

subroutine output(nnx,ny,nx,ny,t,u,v,P,c,mu,k,NT)
implicit none
integer nnx,ny,nx,ny,i,j,k,NT
real *8 t,u,v,P,uVal,vVal,x,y,c,mu
dimension u(1:nnx,0:ny),v(0:nnx-1,1:ny),
#      P(0:nnx-1,0:ny),c(0:nnx-1,0:ny),
#      mu(1:nnx-1,1:ny-1)

if (k.EQ.NT) then
C  WRITE OUT SOLUTION VALUES OVER NODES 1,nx AND 1,ny
do 20 i=1,nx
  x=float(i)
  do 10 j=1,ny
    y=float(j)
    uVal=( u(i,j)+u(i+1,j) )/2.0
    vVal=( v(i,j)+v(i,j+1) )/2.0
    write(2,*)x,y,t,uVal,vVal,P(i,j),c(i,j),mu(i,j)
10  continue
20  continue
  endif
  return
end

```

\*\*\*\*\*

```

subroutine update(nnx,ny,u,v,P,uProv,vProv,Pprov)
implicit none
integer nnx,ny,i,j
real *8 u,v,P,uProv,vProv,Pprov
dimension u(1:nnx,0:ny),uProv(1:nnx,0:ny),
#      v(0:nnx-1,1:ny),vProv(0:nnx-1,1:ny),
#      P(0:nnx-1,0:ny),Pprov(0:nnx-1,0:ny)

do 15 i=1,nnx
  do 10 j=0,ny
    u(i,j)=uProv(i,j)
10  continue
15  continue

```

```

do 25 i=0,nnx-1
  do 20 j=1,nnny
    v(i,j)=vProv(i,j)
20  continue
25  continue

```

```

do 35 i=0,nnx-1
  do 30 j=0,nnny
    P(i,j)=Pprov(i,j)
30  continue
35  continue

```

```

return
end

```

\*\*\*\*\*

```

subroutine converge(nnx,nnny,nx,ny,u,v,uOLD,vOLD,worstv,iv,jv)
implicit none
integer nnx,nnny,nx,ny,i,j,iv,jv
real*8 u,v,uOLD,vOLD,worstv,testv
dimension u(1:nnx,0:nnny), v(0:nnx-1,1:nnny),
#      uOLD(1:nnx,0:nnny),vOLD(0:nnx-1,1:nnny)

```

```

do 20 i=1,nx
  do 10 j=1,ny
    if (u(i,j).NE.0.0) then
      testv=( u(i,j)-uOLD(i,j) )/u(i,j)
    elseif (uOLD(i,j).NE.0.0) then
      testv=( uOLD(i,j)-u(i,j) )/uOLD(i,j)
    endif
    if (testv.GT.worstv) then
      worstv=testv
      iv=i
      jv=j
    endif
    if (v(i,j).NE.0.0) then
      testv=( v(i,j)-vOLD(i,j) )/v(i,j)
    elseif (vOLD(i,j).NE.0.0) then
      testv=( vOLD(i,j)-v(i,j) )/vOLD(i,j)
    endif
    if (testv.GT.worstv) then
      worstv=testv
      iv=i
      jv=j
    endif
    uOLD(i,j)=u(i,j)
    vOLD(i,j)=v(i,j)
10  continue
20  continue

```

```

return
end

```

\*\*\*\*\*

```

subroutine checkmass(nnx,nnny,nx,ny,u,NT)
implicit none
integer nnx,nnny,nx,ny,i,j,NT
real*8 u,mdot,rho

```

```

dimension u(1:nxx,0:nny),mdot(101)

rho=1.0
do 5 i=1,nx
  mdot(i)=0.0
5  continue

do 20 i=1,nx
  do 10 j=1,ny
    mdot(i)=mdot(i)+rho*u(i,j)
10  continue
20  continue

open(unit=62,file='mdot.dat')
rewind(62)
do 30 i=1,nx
  write(62,*)NT,i,mdot(i)
30  continue
rewind(62)
close(62)

return
end

*****

subroutine mixedness(nnx,nny,nx,ny,Mix,c,dx,dy)
implicit none
integer nnx,nny,i,j,nx,ny
real *8 c,Mix,dx,dy
real *8 A,sum0,sum1,sum2,numer,denom1,denom2
dimension c(0:nnx-1,0:nny)

Mix=0.0
A=nnx*ny*dx*dy
numer=0.0
denom1=0.0
denom2=0.0
do 20 i=1,nx
  sum0=0.0
  sum1=0.0
  sum2=0.0
  do 10 j=1,ny
    sum0 = sum0 + c(i,j)*( 1.0-c(i,j) )*dy
    sum1 = sum1 + c(i,j)*dy
    sum2 = sum2 + ( 1.0-c(i,j) )*dy
10  continue
  numer = numer + sum0*dx
  denom1 = denom1 + sum1*dx
  denom2 = denom2 + sum2*dx
20  continue

Mix = (A*numer)/(denom1*denom2)

return
end

*****

```

Subroutine BLT(nnx,nny,nx,ny,u,v,Re,mut,step,nCYCLES.

```

#      Dft,mu,rho,dx,dy,x,y,rads,Zo)
implicit none
integer nnx,nnny,i,j,nx,ny,step,nCYCLES
real*8 u,v,Re,mu,Dft,mu,rho,dx,dy,x,y,rads,Zo,
#      Ccp,Ckleb,Cwake,Ap,ksmall,Kbig,w,mutinner,mutouter,l,
#      rhowall,shearwall,muwall,Ymax,Fmax,Udiff,Fwake,Fwake2,
#      Fkleb,F,Flocal,yPlus,Pr,Le,umax,vmax
dimension u(1:nnx,0:nnny),v(0:nnx-1,1:nnny),
#      Re(1:nnx-1,1:nnny-1),mut(1:nnx-1,1:nnny-1),
#      Dft(1:nnx-1,1:nnny-1),x(0:nnx),y(0:nnny)

Pr = 0.91
Le = 1.0
Ap = 26.0
Ccp = 1.2
Ckleb = 0.65
Cwake = 0.25
ksmall = 0.4
Kbig = 0.0168

do 10, i= 1,nx
  rhowall = rho
  muwall = mu
  shearwall = mu*0.25*( u(i,2)+u(i,ny-1) )
C Find Ymax and Fmax in the transverse direction.
  Ymax = (ny/2)*dy + dy/2.0
  Fmax = 0.0
  umax = 0.0
  vmax = 0.0
  do 6 j = 1,ny
    if (u(i,j).GT.umax) umax = u(i,j)
    if (v(i,j).GT.vmax) vmax = v(i,j)
    yplus = (rhowall*shearwall*Dabs(y(j)))**0.5 / muwall
    w = ( ( ( u(i,j+1)-u(i,j) )/dy
#      - ( v(i+1,j)-v(i,j) )/dx )**2.0)**0.5
    Flocal = y(j)*w*(1.0 - Dexp(-yplus/Ap))
    if (Flocal.GT.Fmax) Ymax = y(j)
    if (Flocal.GT.Fmax) Fmax = Flocal
  6  continue
  do 8, j= 1,ny
C *** First find mutinner ***
    yplus = (rhowall*shearwall*Dabs(y(j)))**0.5 / muwall
    l = ksmall * y(j) * (1.0 - Dexp(-yplus / Ap))
    w = ( ( ( u(i,j+1)-u(i,j) )/dy
#      - ( v(i+1,j)-v(i,j) )/dx )**2.0)**0.5
    mutinner = rho*l*w
C *** Now find mutouter ***
    Udiff = (umax**2 + vmax**2)**0.5
    F = y(j)*w*(1.0-Dexp(-yplus/Ap))
    Fwake = Ymax*Fmax
    Fwake2 = (Cwake*Ymax*Udiff**2)/Fmax
    if (Fwake2.LT.Fwake) Fwake = Fwake2
    Fkleb = (1+5.5*(Ckleb*y(j)/Ymax)**6)**(-1)
    mutouter = Kbig*Ccp*Fwake*Fkleb
C *** Now find mut ***
    if (mutouter.LT.mutinner) then
      mut(i,j) = mutouter
    else
      mut(i,j) = mutinner
    endif
  8  continue
10  continue

```

```
      Re(i,j)=Re(i,j)+mut(i,j)/(rho*Zo*(rads*Zo)**2.0)
C *** Now find the new turbulent diffusion coefficient ****
      Dft(i,j) = Le*mut(i,j)/(Pr*rho)
C *** done with Loop Iteration ***
      8  continue
      10 continue
C *** Fill in last column of variables so output can be viewed on same grid ***
      do 60 j=1,ny
          mut(nnx-1,j)=mut(nx,j)
          Dft(nnx-1,j)=Dft(nx,j)
          Re(nnx-1,j)=Re(nx,j)
      60  continue

      return
      end
```